AIAA JOURNAL
Vol. 46, No. 9, September 2008

Control Input Separation Methods for Reduced-Order Model-Based Feedback Flow Control

Edgar Caraballo,* Coşku Kasnakoğlu,† Andrea Serrani,‡ and Mo Samimy§
The Ohio State University, Columbus, Ohio 43210

DOI: 10.2514/1.35428

First-principle-based models of the dynamics of flow systems are often of limited use for model-based control design, not only because of their nonlinear and infinite-dimensional nature, but also because the control input is generally specified as a boundary condition. Proper orthogonal decomposition and Galerkin projection are among the most effective and commonly used methods to obtain reduced-order models of flow dynamics. However, the final form of these models may not account for the presence of a forcing or control input. From a control design perspective, it is desirable to obtain a reduced-order model in which the control input appears explicitly in the dynamic equations. In this paper, two methods for control input separation are introduced and comparatively evaluated in experimentally based reduced-order modeling of cavity flow, both in their ability to reconstruct the forced flowfield and to provide models suitable for feedback control design. The proposed methods, namely, 1) actuated proper orthogonal decomposition expansion and 2) $\mathcal{L}_2$ optimization, extend the baseline flow model through the use of innovation vectors, which capture the deviation of the actuated flow from the baseline space. The new methods address some of the issues associated with the subdomain separation technique employed in our previous works. Linear-quadratic regulator controllers, built using models obtained from the new methods, have been tested on a cavity flow experiment. Although the new models perform satisfactorily and comparably to our previous models in terms of suppression of cavity tones, they offer a substantial advantage in terms of the required input power to achieve a similar or better performance.

I. Introduction

IT IS typical in flow control problems for the control input to be applied from the physical boundaries of the system. Consequently, when the flow system under investigation is modeled by partial differential equations, the control input appears as a boundary condition, and the resulting control method is usually termed boundary control [1]. Among countless examples of boundary control applied to many different types of dynamic equations, one can find studies in the field of flow control in Gad-el-Hak [2], Aamo and Krstic [3], King [4], and references therein. As for reduced-order modeling for flow control purposes, various techniques have been proposed, ranging from system identification based on experimental data [5–8] to models derived from flow physics [9–13], to cite just a few. Many of these techniques share a common core methodology: starting from the infinite-dimensional governing equations, an optimal set of basis vectors that minimizes the neglected energy in the model is built from flowfield data ("snapshots") obtained from numerical simulations or experimental data. The most common method for obtaining this set of spatial basis functions is the proper orthogonal decomposition (POD) method [14], which decomposes the spatiotemporal evolution of the flowfield into spatial modes and their corresponding modal amplitude. To derive the temporal evolution of the coefficients of the POD expansion, the governing equations are projected onto the space spanned by these bases, a procedure called Galerkin projection (GP), which yields a system of ordinary differential equations that approximates the original dynamics in an energy-optimal sense. A reduced-order model obtained in this fashion is called a Galerkin model (GM) and the methodologies used to obtain such model from the original Navier–Stokes equations are termed model reduction. The POD/GP method is a very common approach to simplify the governing equation from a nonlinear system of functional differential equations to a set of ordinary differential equations that are simpler to manage. This technique has been applied extensively to several flow configurations to obtain reduced-order models, by capturing the evolution of dominant features of the flow such as large-scale structures, which can be used to study the dynamic behavior of the flow [8,12,15]. In recent years, this procedure has been use to develop models amenable for control design purposes [16–20].

Control input separation (or simply input separation) is a method that transforms boundary control to a form that is more useful for control design. The input separation process takes place during model reduction and aims at rendering the presence of the control input explicit in the model. This is the form that is most common when dealing with dynamic systems models for feedback control, and to which the standard tools of control theory can be applied. The methods that have been explored in the literature include techniques such as lifting [21], weak formulation of the Navier–Stokes equations [22,23], balanced truncation [24], and adjoint equations [25]. In the context of POD/GP modeling, Gillies [16] proposed the use of a neural network to obtain an empirical prediction of the effect of external forcing on the temporal evolution of the modal amplitudes of a POD expansion, a technique later adopted and refined by Cohen et al. [26]. For the same purpose, Cohen et al. [27] and Siegel et al. [19] originally employed linear stochastic estimation methods [28]. Noack et al. [12,29] proposed the use of a "shift mode" to account for the transient behavior in reduced-order models of cylinder wakes, and of "actuation modes" (similar to those employed in our study) to account for the actuation.

Control of the flow over a shallow cavity is a benchmark example of boundary flow control that is of great interest from a methodological perspective and in applications alike. This flow is

Received 1 November 2007; revision received 2 May 2008; accepted for publication 4 May 2008.

*Graduate Student, Gas Dynamics and Turbulence Laboratory, Department of Mechanical Engineering. Student Member AIAA.

†Graduate Student, Department of Electrical & Computer Engineering; currently Instructor, Department of Electrical and Electronics, TOBB University of Economics and Technology, Ankara, Turkey.

‡Assistant Professor, Department of Electrical & Computer Engineering. Member AIAA.

§The Howard D. Winbigler Professor of Engineering and Director, Gas Dynamics and Turbulence Laboratory, Department of Mechanical Engineering. Associate Fellow AIAA.

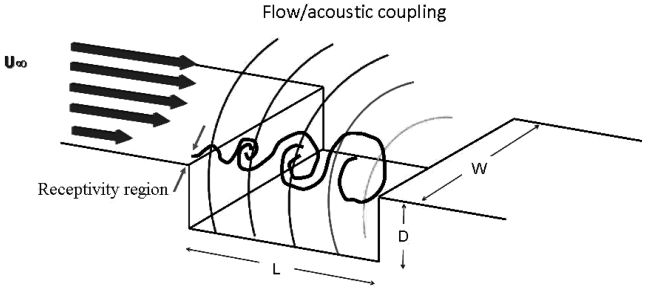

Fig. 1 Schematic of flow over a shallow cavity.

characterized by a strong coupling between flow dynamics and flow generated acoustics that produces a self-sustained resonance (see Fig. 1), which is known to cause, among other problems, structural fatigue in aircraft weapons bays. These characteristics make the cavity flow problem an ideal case study for the development of methodologies for closed-loop flow control of general applicability to other flow configurations. As a result, this problem has been studied extensively in the literature [20,30,31]. The cavity flow control problem has been the main focus of the flow control group at the Gas Dynamics and Turbulence Laboratory (GDTL) at The Ohio State University (OSU) over the last few years, with significant effort devoted to the development of model-based feedback control [20,32,33]. In particular, the POD/GP approach to control-oriented reduced-order modeling has been explored in Samimy et al. [20] and Caraballo et al. [34], where the control input was made explicit in the Galerkin model by means of subdomain separation methods [35,36].

Even though our focus has been directed to cavity flows, our goal has been to develop methodologies that can be applied to the control of other flow configurations. Having already obtained controllers that work successfully in experiments, the group is currently working on improving the design and establishing mathematical and theoretical foundations for the key components of the closed-loop system. In an attempt to take a step further in this direction, it has been found that, among the major elements in the design and implementation of a feedback controller, control input separation is a key issue that needs to be rethought and redesigned. Although the aforementioned method for input separation provides a means to obtain the input as an explicit term, there are major issues associated with it, especially from a theoretical point of view, and much room for improvement. First of all, the separation is performed at the level of the Galerkin projection after the generation of a POD basis from flow images, which include snapshots of baseline flow, actuated flow, or combinations of the two. Although the inclusion of snapshots of actuated flow is required to process data for identification that capture the effect of external forcing, it nevertheless creates a bias in the model, which limits its ability to reproduce the unforced baseline case when the input is set to zero. Similarly, the resulting reduced-order model is not capable of reconstructing correctly the individual forced flows when the control input term was included. This is somehow expected, as the POD basis obtained with this approach tends to capture the evolution of the forcing input itself rather than the effects it produces on the flowfield, because the generation of the POD basis can not distinguish between the two. For the same reason, the model is not capable of representing flow conditions for inputs which are different from the ones used to generate the snapshots used to build the model. This limitation is also related to the fundamental and long-standing issue related to the selection of the most appropriate combination of external forced conditions to be used for system identification of reduced-order models of flow systems. Finally, a problem specific to the particular technique adopted in the subdomain separation method regards the necessity of identifying a specific control input region in the spatial domain, where the control input acts as a boundary condition, which may not be possible for some flow configurations.

In this paper, we explore two alternative control input separation methods which rely upon an expansion of the flowfield in terms of baseline POD modes and actuation modes, where the former is derived from snapshots of the baseline flow and the latter from actuated flow data. The idea of adding actuation modes to the POD expansion draws inspiration from the concepts of shift mode and interpolated POD modes developed by Noack et al. [12,37]. To obtain the actuation modes, the approach proposed in this paper uses a concept of "innovation flowfield" similar to the split-POD employed by Camphouse [38], where a finite-dimensional approximation of the subspace orthogonal to the one spanned by baseline POD modes was also employed to construct the overall set of basis functions. However, the approach taken in [38] differs from the ones proposed herein in the use of weak formulation to render the control input explicit in the Galerkin system.

It is shown that the proposed methods address to a satisfactory extent the problems associated with the previous approach, while being more theoretically sound. In addition, by using several inputs for system identification, an inquiry is made about the best selection of forcing conditions to be used in the derivation of the reduced-order model.

The paper is organized as follows. Section II introduces the cavity flow experimental setup. Section III presents the motivations for this study. Section IV explains the new separation methods in detail. Section V provides experimental verification of the methods by illustrating their capabilities in providing a reconstruction of the flowfield and in generating models which are appropriate for feedback control. Section VI provides concluding remarks.

II. Cavity Flow Experimental Setup

In this section, a brief description of the experimental setup located at The Ohio State University Gas Dynamics and Turbulence Laboratory is summarized. The complete details of the experimental setup can be found in [20,39]. The experimental facility is an instrumented, optically accessible wind tunnel that operates in a blowdown fashion with atmospheric exhaust. The air is conditioned in a stagnation chamber before entering a smoothly contoured converging nozzle to the 50.8 mm × 50.8 mm test section, and can run continuously in the subsonic range between Mach 0.25 and 0.70. The test section contains a shallow cavity with a depth $D = 12.7$ mm and length $L = 50.8$ mm for an aspect ratio $L/D = 4$. For control purposes, a 2-D synthetic jet-type actuator is used to force the cavity shear layer at its receptivity region. The forcing is issued at 30 deg relative to the main flow from a 1 mm slot embedded in the cavity leading edge that spans the width of the cavity (see Fig. 2a). The mechanical oscillations necessary for the flow actuation are provided by a selenium D3300Ti compression driver. The actuation jet has a zero net mass, nonzero net momentum flow.

A LaVision, Inc., particle imaging velocimetry (PIV) system [40] is used to acquire the snapshots of the flowfield required for the development of the low-dimensional model. A dual-head Spectra Physics PIV-400 Nd:YAG laser operating at the second harmonic (532 nm) is used to form a thin (1 mm), vertical sheet spanning the streamwise direction of the cavity at the middle of the test section width. The time separation between the laser pulses for the flow at Mach 0.30 in our experimental setup is 1.8 μs. For each image, subregions are cross correlated by using multipass processing with 50% overlap. The resulting vector fields are postprocessed to remove any remaining spurious vectors. This setup gives a velocity vector grid with vector separation of approximately 0.4 mm.

Dynamic surface pressure measurements are taken with flush-mounted Kulite transducers placed at various locations on the walls of the test section. Figure 2b shows the locations of the transducers used in this study. The signal from the transducers are low-pass filtered at 10 kHz. These pressure measurements are recorded simultaneously with the PIV measurements, using a National Instruments PCI-6143 S-series data acquisition board, and are used for state estimation. For each flow/actuation condition explored, 1000 PIV snapshots are recorded. Correspondingly, for each PIV snapshot, 128 pressure samples from the laser Q-switch signal and from each of the transducers of Fig. 2b are acquired at 50 kHz. The system is programmed for the PIV image to fall approximately in the middle of the 128 pressure data points. This simultaneous sampling allows for the identification of the section of pressure time traces that

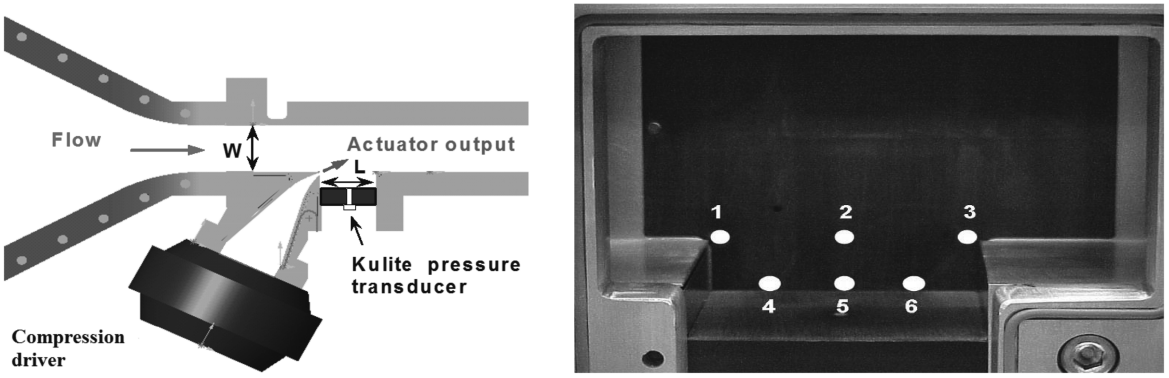

a) Scaled drawing of the experimental setup

b) Location of Kulite pressure transducers on the side wall of the test section

Fig. 2 Schematics of the OSU GDTL cavity flow experimental setup.

corresponds to the instantaneous PIV velocity field. Additional, longer recordings of 262,144 samples per channel acquired at 200 kHz were also used to derive sound pressure level (SPL) spectra.

A dSPACE DS1103 PPC controller board is used for real-time feedback control. This system uses four independent, 16-bit A/D converters each with four multiplexed input channels to acquire and process signals at a rate up to 50 kHz per channel. The pressure signals are also bandpass filtered between 100 Hz and 10 kHz to remove spurious frequency components.

The dynamic compensator developed in Kim et al. [33] has been employed to shape the frequency response of the synthetic-jetlike actuator. The compensator increases the loop gain and suppresses the unfavorable frequency peaks in the actuator response due to the internal acoustic phenomena associated with the converging nozzle. As a result, the actuator response in the frequency domain can be considered to be approximately flat in the region of interest (1–5 kHz). This makes it possible to effectively use a band-limited white noise signal as input voltage to the actuator to force the flow in the cavity.

III. Motivations for the Study

In this section, the motivations behind this study are highlighted by first providing a summary of the POD/GP approach to obtain a reduced-order model of the cavity flow, and pointing out the difficulties encountered from a control theory perspective. Then, the subdomain separation method used in our previous studies [20,34] is briefly reviewed to provide a comparison with the methodology developed and presented herein.

A. Proper Orthogonal Decomposition/Galerkin Projection Based Modeling

The dynamics of the cavity flow are described by the Navier–Stokes equations. Although the baseline flow employed in our studies is around the incompressible limits (Mach 0.3), the compressible form of the equations were used for the derivation of a model of general validity. The flow was treated as isentropic to simplify the final form of the system. Following the procedure presented by Rowley et al. [41], the compressible form of the Navier–Stokes (NS) equations can be written as

$$\frac{\mathrm{D}\boldsymbol{u}}{\mathrm{D}t}+\frac{1}{M^2}\frac{2}{\kappa-1}\nabla c=\frac{1}{Re}\nabla^2\boldsymbol{u}\qquad \frac{\mathrm{D}c}{\mathrm{D}t}+\frac{\kappa-1}{2}c\mathrm{div}\boldsymbol{u}=0 \tag{1}$$

where $\boldsymbol{u}(\boldsymbol{x},t)=(u(\boldsymbol{x},t),v(\boldsymbol{x},t))$ is the flow velocity in the streamwise and normal direction, $c(\boldsymbol{x},t)$ is the local speed of sound, the operator $\mathrm{D}/\mathrm{D}t=\partial/\partial t+\boldsymbol{u}\cdot\nabla$ stands for the material derivative, and $\boldsymbol{x}=(x,y)$ denotes Cartesian coordinates over the spatial domain $\Omega\subset\mathbb{R}^2$. The constants κ, Re, and M denote, respectively, ratio of specific heats, Reynolds number, and Mach number. These equations can be expressed in compact form as the functional differential equation

$$\dot{\boldsymbol{q}}=X(\boldsymbol{q}):=\boldsymbol{C}+\boldsymbol{L}(\boldsymbol{q})+\boldsymbol{Q}(\boldsymbol{q},\boldsymbol{q}) \tag{2}$$

defined on the Hilbert space $\mathbb{H}=\mathcal{L}_2(\Omega,\mathbb{R}^3)$ of square-integrable functions on Ω, where $\boldsymbol{q}:=(u-u_0,v-v_0,c-c_0)\in\mathbb{H}$ is the fluctuations of the flow velocity about the mean value $\boldsymbol{q}_0=(u_0,v_0,c_0)$. In Eq. (2), $\boldsymbol{C}$ is a constant operator, $\boldsymbol{L}$ is a linear operator, and $\boldsymbol{Q}(\boldsymbol{q},\boldsymbol{q})$ is quadratic in $\boldsymbol{q}$. For convenience of the reader, a brief summary on the derivation of this compact form can be found in Appendix A. The reader interested in the full details is referred to [41].

The POD/GP procedure decomposes the flowfield vectors to a small number of spatial orthogonal modes, $\phi_i(\boldsymbol{x})$, $i=1,\ldots,N$, that capture the spatial distribution of the structures and the corresponding modal amplitude coefficients a_i that capture the temporal evolution of these modes. This set of modes retains the largest portion of the kinetic energy of the flow as defined by the inner product being used [14,41]. To compute the POD basis, Sirovich's method of snapshots [42] is applied. Measurements of the flow velocity field $\boldsymbol{u}(\boldsymbol{x}_i,t_j)$ are acquired using PIV over a spatial discretization of the domain Ω. The corresponding values of the local speed of sound $c(\boldsymbol{x},t)$ are computed from the local temperature $T(\boldsymbol{x},t)$ using the relation $c=(\kappa RT)^{1/2}$, whereas the local temperature is obtained again from the flow velocity, noticing that for isentropic flows $c_pT_0=c_pT(\boldsymbol{x},t)+\|\boldsymbol{u}(\boldsymbol{x},t)\|^2/2$, where c_p is the specific heat at constant pressure and T_0 is the measured stagnation temperature. Once the POD modes ϕ_i have been obtained, the fluctuating component of the flowfield can be represented as the finite-dimensional approximation defined by

$$\boldsymbol{q}(\boldsymbol{x},t)\approx\sum_{i=1}^{N}a_i(t)\phi_i(\boldsymbol{x}) \tag{3}$$

For the sake of simplicity, Einstein summation notation will be used when convenient, and summation signs will be omitted. Then, Eq. (3) becomes $\boldsymbol{q}(\boldsymbol{x},t)\approx a_i(t)\phi_i(\boldsymbol{x})$. The Galerkin projection method is used to obtain a differential equation governing the evolution of the modal amplitudes. This is achieved by replacing the flow variables in the NS equation by the POD expansion, and projecting the modified system onto the POD modes, using the inner product definition. The final form of the system corresponds to a set of ordinary differential equations (ODEs) that is truncated to a desired number of modes, based on the specific application. After all the simplifications are carried out, the Galerkin system can be expressed as

$$\dot{a}_k=F_k+G_{ik}a_i+H_{ijk}a_ia_j,\qquad k=1,\ldots,N \tag{4}$$

where F_k, G_{ik}, and H_{ijk} depend on parameters in Eq. (2).

It has been noted [34] that the solution of the system (4) often diverges independently of the initial condition used. This has been attributed to numerical errors in the spatial derivative terms present in system (4) and to the finite number N of modes retained to describe the flow. This reduced set not only loses some flow details, but also fails to capture the process of energy transfer between the N retained

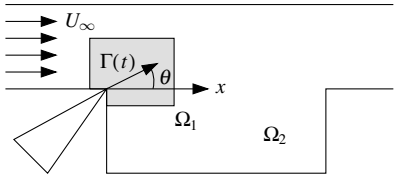

Fig. 3 Subdomain control input separation method.

modes and those that are neglected. This can be corrected by the introduction of an additional viscous term, the modal eddy viscosity. The details of its implementation to the current work can be found in Caraballo et al. [34]. The addition of this viscosity term to the model helps in maintaining the overall flow energy balance, and it also compensates for other small errors introduced in the derivation of the model. From this point on, the viscous term will be included in all the models derived even if there is no explicit mention to it.

At this point, it is clear that the effect of actuation is contained in the coefficients of the Galerkin system (4), and does not appear explicitly as a separate term on the right-hand side of the equation. To remedy this situation, in our previous work [20,34], the so-called subdomain input separation method [35,36] was applied. Here, we will limit ourself to providing a brief summary of the method, highlighting the issues encountered that promoted the need to pursue alternative methodologies.

B. Subdomain Separation Method (M0)

The subdomain separation method is based on a special treatment of the boundary elements of the spatially discretized governing equations. The procedure takes advantage of the linear property of the inner product by dividing the entire flow domain into two subdomains, so that $\Omega = \Omega_1 \cup \Omega_2$, as shown in Fig. 3. The smaller domain Ω_1 comprises the physical region where the actuation enters the flowfield, and the larger region Ω_2 contains the rest of the flowfield. Input separation was performed during the Galerkin projection implementation by splitting the inner product as

$$\langle \cdot, \cdot \rangle_\Omega = \langle \cdot, \cdot \rangle_{\Omega_1} + \langle \cdot, \cdot \rangle_{\Omega_2}$$

Then, the boundary conditions are imposed on Ω_1. This involves repartitioning the domain by changing the limits of a Riemann integral computed over nonoverlapping subdomains embodying the domain of the original integral when they are united. The procedure yields a nonautonomous set of ODEs in the following form:

$$\dot{a}_k = F_k + G_{1ik} a_i + g_{2k} \Gamma + H_{1ijk} a_i a_j + H_{2ik} a_i \Gamma \qquad (5)$$

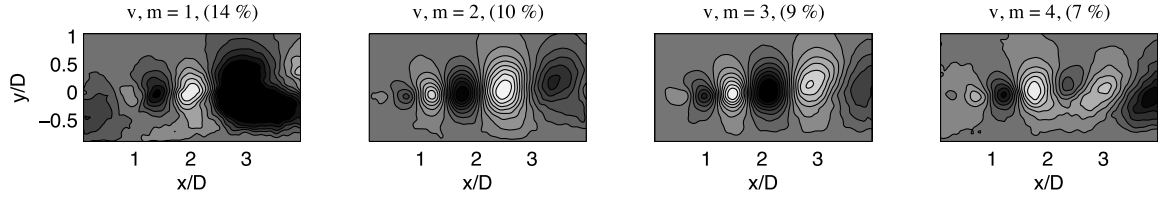

a) Baseline flow (Mach 0.3)

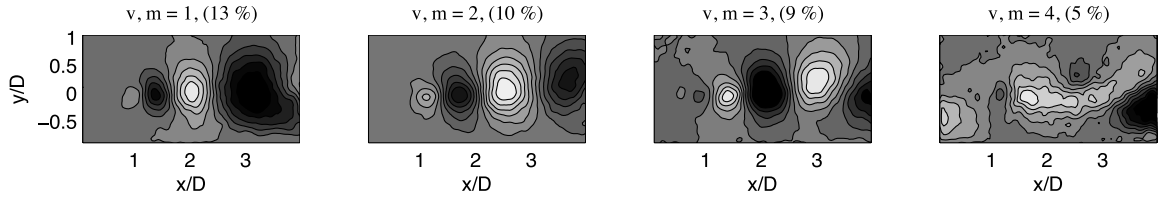

b) Open-loop forcing at f = 3920 Hz (F4)

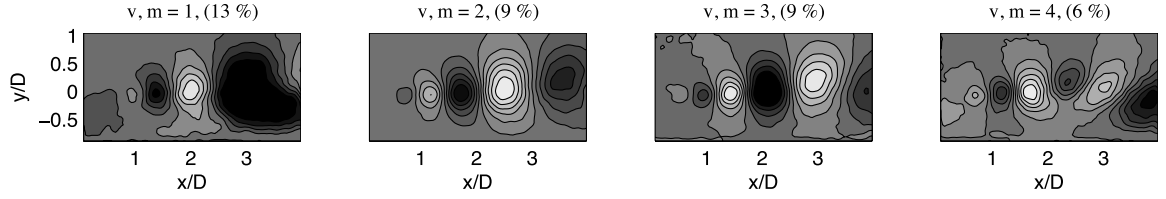

c) Baseline and F4 combined (BF4)

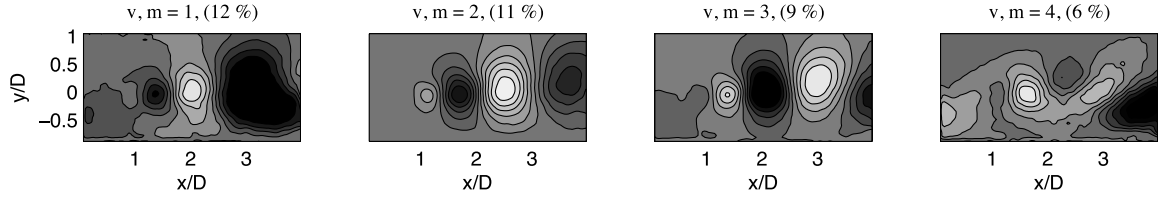

d) Baseline, open-loop forcing at f = 1610 Hz (F1), and F4 combined (BF1F4)

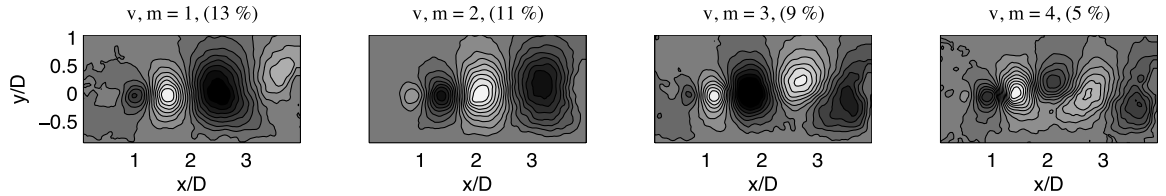

e) Band-limited white noise forcing (Wn)

Fig. 4 POD modes of the different flow conditions used for the development of the reduced-order models.

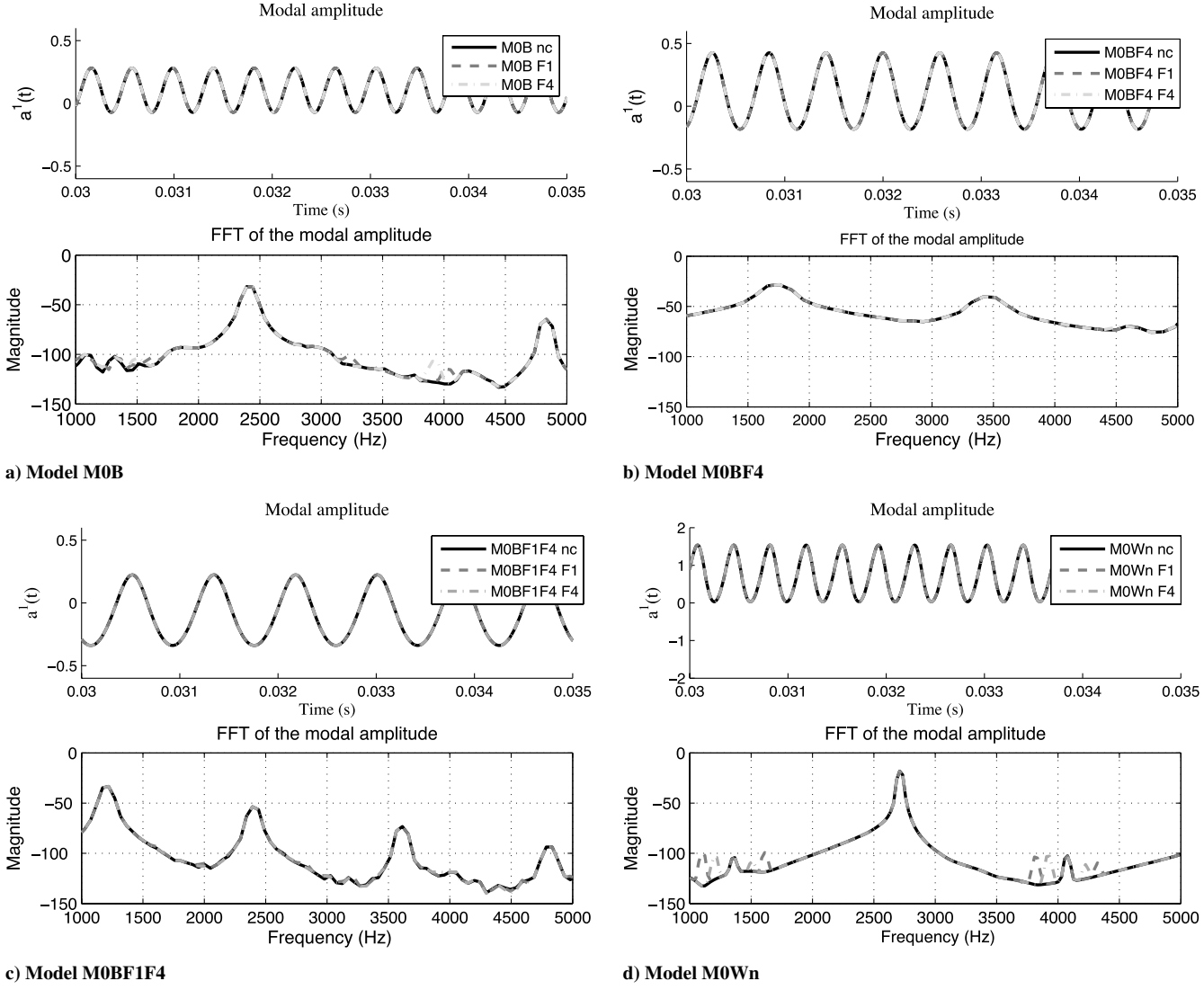

Fig. 5 Time series and power spectrum of the first modal amplitude of the Galerkin system obtained using subdomain input separation. The second label represents the external input applied to the Galerkin model in nonlinear simulations: nc (no control), F1 ($f = 1610$ Hz), and F4 ($f = 3920$ Hz).

where Γ is the external input, which in our studies is given by the voltage applied to the synthetic-jetlike actuator. Further details on the application of this separation method to the cavity flow control problem can be found in the aforementioned references.

As mentioned in the Introduction, although the subdomain separation method provides a means to obtain the control input term explicitly, there are still several important issues associated with this procedure that surfaced during the derivation, implementation, and experimental evaluation of the reduced-order models. First, the procedure requires an identifiable region in the flow where the forcing is introduced, which may be difficult in many flow configurations. Second, the separation is performed after the POD basis of the entire flowfield is obtained. The forcing effect is embedded within the PIV snapshots used to derive the model, and thus the POD modes derived from snapshots of actuated flow are dependent on the data set used in the derivation. Figure 4 shows the first four POD modes of several models based on the M0 method corresponding to various forcing conditions, including the baseline flow.[¶] Although the spatial evolution of the POD modes exhibit a change as a result of the actuation, the Galerkin model does not show any significant correlation between the control input and the modal coefficients $a_i(t)$. This issue can be clearly observed in Fig. 5, which shows the numerical solution of the Galerkin system (5) obtained using different combinations of baseline and actuated data sets (models M0B, M0BF4, M0BF1F4, and M0Wn) when forced by sinusoidal signals at frequency $f = 1610$ Hz (F1) and $f = 3920$ Hz (F4). It can be noted that the addition of the forcing term does not show any effects on the amplitude and/or frequency of the modal coefficient. This was observed independent of the model or forcing frequency used. This creates a mismatch in scale between values obtained in simulation for the control and its actual value to be used in real-time experiments. In our previous studies, the amplitude of the forcing term had to be increased up to 100 times for the solution of system (5) to show any significant change. This phenomenon is clearly related to a severe underestimation of the magnitude of control vector field in the reduced-order model. Naturally, it was speculated that the source of the problem lies within the method for control separation adopted in the construction of the reduced-order model.

IV. Alternative Approaches to Input Separation

To address the issues discussed in the previous section, two alternative approaches were developed to separate the control from the boundary conditions. Both methods treat the control input as additional terms in the POD expansion by means of actuation modes.

[¶]Each individual case is indicated in the nomenclature used for the model by adding the corresponding forcing after the method name. For instance, M0B refers to the initial model based on the baseline flow case, M0BF4 to the M0 method based on combination of baseline and F4 snapshots, and so on. The nomenclature is consistent with the one adopted in [20] (see Table 1).

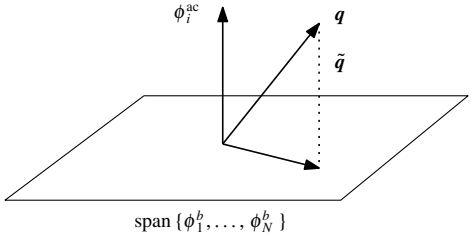

Fig. 6 Graphical representation of baseline POD subspace, innovation, and actuation modes.

The first method (M1) is based on an augmented POD expansion of the actuated flow and relies upon stochastic estimation to correlate the modal coefficients of the actuation modes to the input. In the second method (M2), which is based on $\mathcal{L}_2$ optimization, the control input enters directly as a modal coefficient of an optimally selected spatial mode. As the two methods have several features in common, we will first start by defining concepts that are common to both approaches. Then, each approach will be discussed in more detail and compared.

A. Basic Concepts

The basic idea behind the new approaches is to introduce the presence of control input in the process before the Galerkin procedure is applied. This is accomplished by complementing the set of baseline POD modes in the POD approximation of the flowfield fluctuations with additional actuation modes that have the role of resolving the variation of the flowfield due only to the affect of external forcing.

In the approach considered in this paper, first, a set of baseline modes $\phi_i^b(\boldsymbol{x})$ are determined from snapshots of the baseline flow, that is, the case when $\Gamma = 0$ as shown in Fig. 4a. Given snapshots of the actuated flow fluctuations $\boldsymbol{q}(\boldsymbol{x}, t)$, the innovation $\tilde{\boldsymbol{q}}(\boldsymbol{x}, t)$ is defined as

$$\tilde{\boldsymbol{q}}(\boldsymbol{x}, t) := \boldsymbol{q}(\boldsymbol{x}, t) - P_S \boldsymbol{q}(\boldsymbol{x}, t) \tag{6}$$

where $S := \text{span}\{\phi_i^b\}_{i=1,\ldots,N}$ and P_S is the standard projection operator onto S. The innovation represents the information contained in the actuated flow that can not be captured by S. Figure 6 provides a graphical illustration of this concept. A set of actuation modes $\phi_i^{ac}(\boldsymbol{x})$, $i = 1, \ldots, N_{ac}$ can then be constructed from snapshots of the innovation, using one of the two methods to be described next. As a result, the flowfield can be represented using an expansion of the form

$$\boldsymbol{q}(\boldsymbol{x}, t) \approx \sum_{i=1}^{N} a_i^b(t)\phi_i^b(\boldsymbol{x}) + \sum_{i=1}^{N_{ac}} a_i^{ac}(t)\phi_i^{ac}(\boldsymbol{x}) \tag{7}$$

where $a_i^{ac}(t) = \langle \boldsymbol{q}, \phi_i^{ac} \rangle$. Ideally, the innovation vanishes in the absence of external forcing, and thus the baseline flow should be recovered in an expansion along baseline modes when $\Gamma(t) = 0$. As a result, the modal amplitudes associated with the actuation modes should vanish as well. The procedure to construct the basis functions $\phi_i^{ac}(\boldsymbol{x})$, and the way the amplitudes $a_i^{ac}(t)$ are related to $\Gamma(t)$, constitute the difference between the two methods described in the next sections.

B. Actuation Modes Based on POD Expansion of the Innovation (M1)

The first method to obtain the actuation modes relies upon a POD expansion of innovation flow data, followed by a stochastic estimation procedure to correlate the modal amplitudes with the external input. Once the baseline POD modes ϕ_i^b are built and the innovation is constructed, as described in Sec. IV.A, the modes ϕ_i^{ac} are determined using the POD procedure from snapshots $\tilde{\boldsymbol{q}}_k = \tilde{\boldsymbol{q}}(\boldsymbol{x}, t_k)$. Although, by definition, the actuation modes should be orthogonal to the baseline modes, the Gram–Schmidt procedure is then used to make sure that the orthonormality condition is satisfied among all modes. Figure 7 shows the control modes $\{\phi_i^{ac}\}_{i=1}^{N_{ac}}$, where $N_{ac} = 4$, computed under three different actuations: F4, F4 and F1 combined, and white noise. It can be observed that the modes obtained from white noise forcing have a more random spatial distribution, with no defined number of structures present, whereas the other two cases show the presence of structures (identified by pairs of dark and light contours) along the shear layer region. The next step is the correlation of the actual forcing input with the actuation mode coefficients in Eq. (7). The voltage input to the actuator is the most natural choice for the forcing input, as in

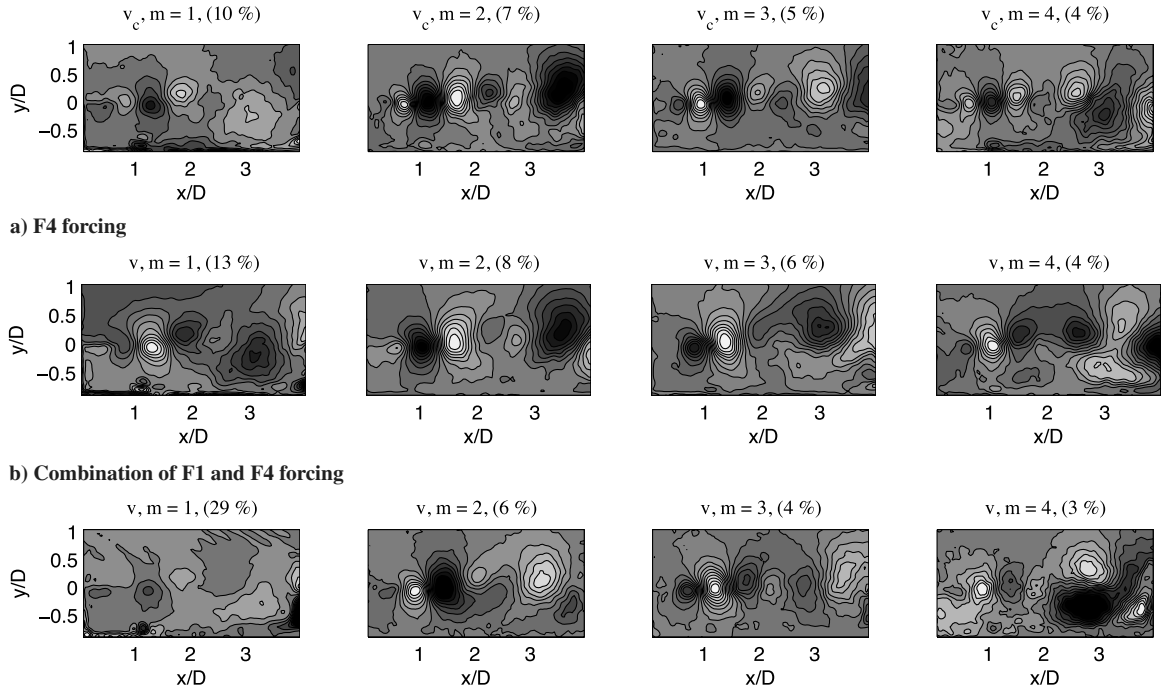

Fig. 7 Control modes for separation method M1, based on different forcing conditions.

closed-loop operations it represents the actual control signal sent into the system, as computed by the feedback controller. For the purpose of correlating $a_i^{\mathrm{ac}}(t)$ with $\Gamma(t)$, a quadratic stochastic estimation procedure [28,34,43,44] is employed, yielding an expression of the form

$$a_i^{\mathrm{ac}}(t) \approx M_i\Gamma(t) + O_i\Gamma(t)^2 \tag{8}$$

where M_i and O_i are, respectively, the coefficients of the linear and quadratic terms of the estimator. Once the coefficients of Eq. (8) are computed by least-squares optimization, substitution of Eq. (8) into Eq. (7) yields

$$\begin{aligned}\boldsymbol{q}(\boldsymbol{x},t) &\approx \sum_{i=1}^{N} a_i^b(t)\phi_i^b(\boldsymbol{x}) + \sum_{i=1}^{N_{\mathrm{ac}}}[M_i\Gamma(t) + O_i\Gamma(t)^2]\phi_i^{\mathrm{ac}}(\boldsymbol{x}) \\ &= \sum_{i=1}^{N} a_i^b(t)\phi_i^b(\boldsymbol{x}) + \Gamma(t)\psi_1(\boldsymbol{x}) + \Gamma(t)^2\psi_2(\boldsymbol{x})\end{aligned} \tag{9}$$

where

$$\psi_1(\boldsymbol{x}) := \sum_{i=1}^{N_{\mathrm{ac}}} \phi_i^{\mathrm{ac}}(\boldsymbol{x})M_i, \qquad \psi_2(\boldsymbol{x}) := \sum_{i=1}^{N_{\mathrm{ac}}} \phi_i^{\mathrm{ac}}(\boldsymbol{x})O_i$$

are the final expressions on the actuation modes with temporal coefficients expressed in terms of the external input. Once the final form [Eq. (9)] of the POD expansion is obtained, Galerkin projection is performed on the governing equations, yielding a Galerkin model of the form

$$\begin{aligned}\dot{a}_k = {} & F_k + G_{1ik}a_i + g_{2k}\Gamma + H_{1ijk}a_ia_j + H_{2ik}a_i\Gamma \\ & + (h_{3k} + g_{3k})\Gamma^2 + H_{3ik}a_i\Gamma^2 + h_{4k}\Gamma^3 + h_{5k}\Gamma^4\end{aligned} \tag{10}$$

where

$$F_k = \left\langle \boldsymbol{C}, \phi_k^b \right\rangle, \qquad G_{ik} = \left\langle \boldsymbol{L}\left(\phi_i^b\right), \phi_k^b \right\rangle$$

$$g_{2k} = \left\langle \boldsymbol{L}(\psi_1), \phi_k^b \right\rangle, \qquad g_{3k} = \left\langle \boldsymbol{L}(\psi_2), \phi_k^b \right\rangle$$

$$H_{1ijk} = \left\langle \boldsymbol{Q}\left(\phi_i^b, \phi_j^b\right), \phi_k^b \right\rangle$$

$$H_{2ik} = \left\langle \boldsymbol{Q}\left(\phi_i^b, \psi_1\right), \phi_k^b \right\rangle + \left\langle \boldsymbol{Q}\left(\psi_1, \phi_i^b\right), \phi_k^b \right\rangle$$

$$H_{3ik} = \left\langle \boldsymbol{Q}\left(\phi_i^b, \psi_2\right), \phi_k^b \right\rangle + \left\langle \boldsymbol{Q}\left(\psi_2, \phi_i^b\right), \phi_k^b \right\rangle$$

$$h_{3k} = \left\langle \boldsymbol{Q}\left(\psi_1, \psi_1\right), \phi_k^b \right\rangle, \qquad h_{4k} = \left\langle \boldsymbol{Q}(\psi_1, \psi_2), \phi_k^b \right\rangle$$

$$h_{5k} = \left\langle \boldsymbol{Q}(\psi_2, \psi_2), \phi_k^b \right\rangle$$

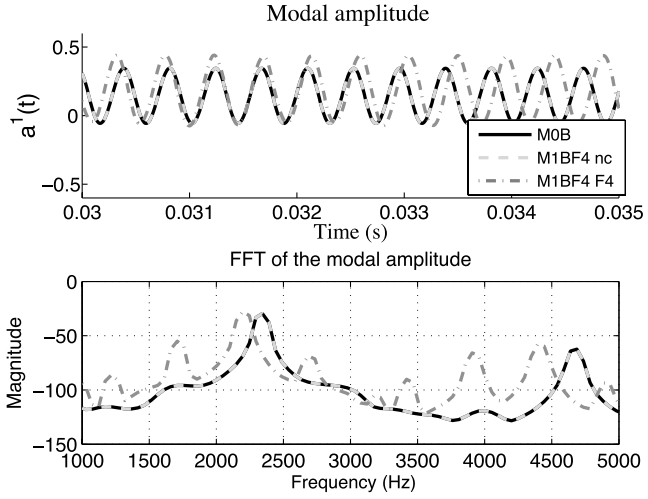

a) Model M1BF4

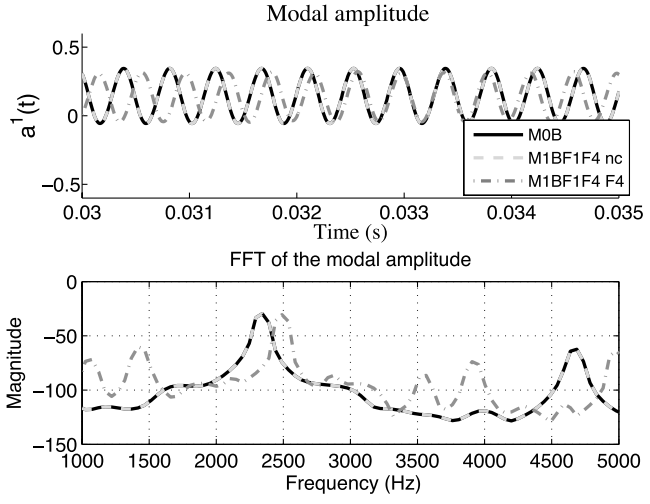

b) Model M1BF1F4

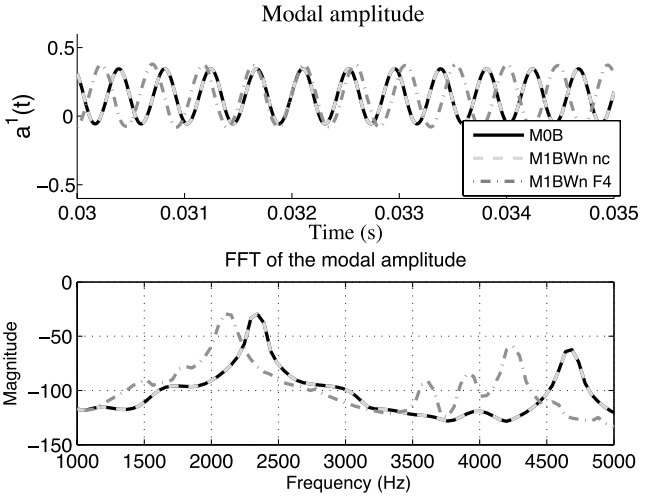

c) Model M1Wn

Fig. 8 Time series and power spectrum of the first modal amplitude of the Galerkin system obtained using method M1. Results for the baseline model M0B are reported for comparison.

Now that the model is complete, one can solve system (10) numerically to test its behavior under different forcing inputs. Figure 8 shows the numerical solution of the preceding Galerkin system for three different models, based on the flow conditions used. It can be observed that when the control is not present (nc), the solution of the different systems match the baseline case solution (M0B), as desired. When forcing is introduced (for example, case F4), a change is noticed in the amplitude and frequency of the modal coefficients. This is observed for all the combinations tested. This seems to address the sensitivity issue of the initial model (M0), where no difference was observed when the forcing was introduced into the system in simulation.

C. $\mathcal{L}_2$ Optimization (M2)

The second method that was developed relies on defining and solving an optimization problem so as to identify a single actuation mode ψ to augment the POD expansion, in such way that the system input is directly the coefficient of ψ. To elaborate, the expansion sought is of the form

$$\boldsymbol{q}(\boldsymbol{x}) \approx \sum_{i=1}^{N} a_i^b(t)\phi_i^b(\boldsymbol{x}) + \Gamma(t)\psi^*(\boldsymbol{x}) \tag{11}$$

where the actuation mode ψ^* is to be chosen so as to minimize the energy not captured by such an expansion. The rest of this section will introduce this idea formally.

The first step consists of obtaining the baseline POD modes ϕ_i^b and building the innovations $\tilde{\boldsymbol{q}}$, as described in Sec. IV.A. Then, an optimization problem on the Hilbert space $\mathbb{H}$ is defined as

$$\psi^* = \arg\min_{\psi\in\mathbb{H}} E\{\|\tilde{\boldsymbol{q}}_k - \Gamma_k\psi\|^2\} \tag{12}$$

where $(\tilde{\boldsymbol{q}}_k, \Gamma_k) = (\tilde{\boldsymbol{q}}(\boldsymbol{x}, t_k), \Gamma(t_k))$ are snapshots of the innovation and the corresponding forcing input, $E\{\cdot\}$ denotes temporal averaging, and the norm is the one induced by the inner product on $\mathbb{H}$. The solution of the optimization problem ψ^* is chosen as the actuation mode. Therefore, among all augmented POD expansions in the form given in Eq. (11), where the input Γ directly appears as the coefficient of ψ, the choice $\psi = \psi^*$ is optimal in the sense that the energy not captured by this expansion achieves there its minimum value. The following theorem summarizes the main result:

Theorem IV.1. Let $J(\psi) := E[\|\tilde{\boldsymbol{q}}_k - \Gamma_k\psi\|^2]$. Then,

1) The minimum value of the function J is achieved at

$$\psi^* = \frac{E[\Gamma_k\tilde{\boldsymbol{q}}_k]}{E[(\Gamma_k)^2]}$$

2) For $\psi^* \in \mathbb{H}$.

3) For $\psi^* \perp \phi_i$ for $i = 1, \ldots, N$.

For a proof of Theorem IV.1, see Appendix B.

It is worth noting that, similar to the method of snapshots, the infinite-dimensional optimization problems in Eq. (12) admits a finite-dimensional solution. Galerkin projection of the NS Eqs. (4) onto the subspace spanned by ϕ_i^b, $i = 1, \ldots, N$ and ψ^* yields a Galerkin model of the form

$$\dot{a}_k = F_k + G_{1ik}a_i + g_{2k}\Gamma + H_{1ijk}a_ia_j + H_{2ik}a_i\Gamma + h_{3k}\Gamma^2 \tag{13}$$

where

$$F_k = \left\langle \boldsymbol{C}, \phi_k^b \right\rangle, \qquad G_{1ik} = \left\langle \boldsymbol{L}\left(\phi_i^b\right), \phi_k^b \right\rangle, \qquad g_{2k} = \left\langle \boldsymbol{L}(\psi^*), \phi_k^b \right\rangle$$

$$h_{3k} = \left\langle \boldsymbol{Q}(\psi^*, \psi^*), \phi_k^b \right\rangle \qquad H_{1ijk} = \left\langle \boldsymbol{Q}\left(\phi_i^b, \phi_j^b\right), \phi_k^b \right\rangle$$

$$H_{3ik} = \left\langle \boldsymbol{Q}\left(\phi_i^b, \psi^*\right), \phi_k^b \right\rangle + \left\langle \boldsymbol{Q}\left(\psi^*, \phi_i^b\right), \phi_k^b \right\rangle$$

Figure 9 shows the control mode ψ^* computed under three different actuations: F4, F4 and F1 combined, and white noise (Wn). Again, the mode obtained using white noise excitation shows no defined structures, whereas the mode based on sinusoidal forcing

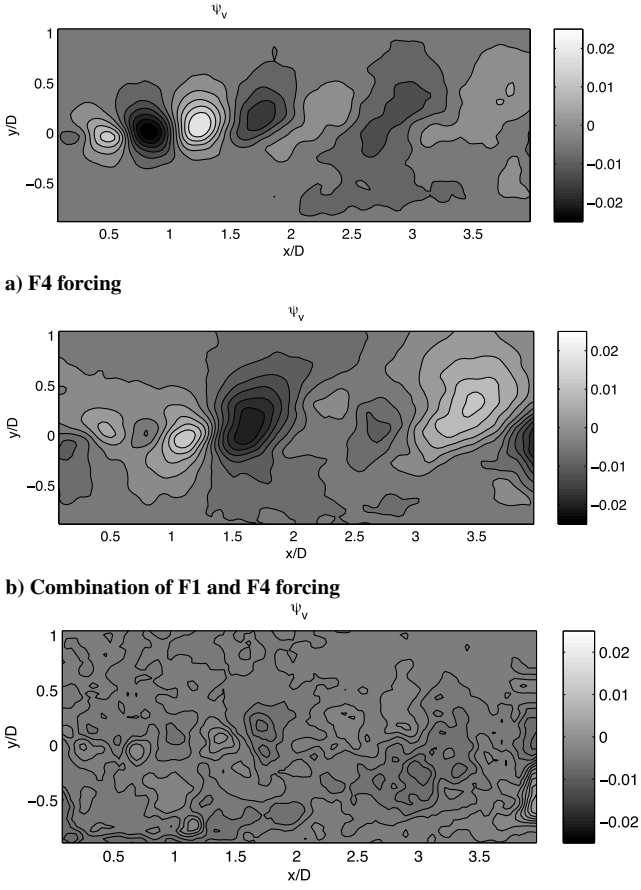

Fig. 9 Control mode ψ^* for separation method M1, based on different forcing conditions.

contains well-defined structures around the shear layer region. The sensitivity of model M2 to the forcing input can be now tested numerically, as done previously with model M1. Figure 10 shows the results of the numerical solution of the Galerkin models M2BF4, M2BF1F4, and M2BWn corresponding to the three different data sets used for system identification. The results obtained with this method are similar to the ones obtained with the previous model: When no external input is applied (nc), the solution of the Galerkin systems matches the baseline case solution (M0B). However, when forcing is introduced (i.e., F4), there is a noticeable change in the amplitude and spectrum of the modal coefficient.

D. Comparison Between the Proposed Approaches

A first comparison between the two methods regards the structure of the Galerkin systems given by Eqs. (10) and (13), respectively. It is worth noting that the coefficients of the so-called drift vector field (that is, F_k, G_{1ik}, and H_{1ijk}) are the same for the two models, because they are obtained from the same baseline snapshots. The difference resides in the control-dependent terms. The cubic and quartic terms in Γ appearing in Eq. (10), not present in Eq. (13), are due to the choice of a quadratic estimation method to correlate the temporal coefficients $a_i^{\mathrm{ac}}(t)$ to the forcing input $\Gamma(t)$. Setting $O_i = 0$, the estimation expression in Eq. (8) reduces to a linear stochastic estimation, which yields for M1 a reduced-order model of the same form of Eq. (13), albeit with different coefficients. In this regard, it is useful to compare the two models in the case that a linear estimation is adopted for M1. Because the choice $\psi = \psi^*$ is optimal (in the sense that the mean-squared error is minimized), the model M2 is expected to yield a better approximation of the flow variables over any POD expansion of the form of Eq. (11), including the one in which ψ is obtained by means of linear stochastic estimation, as in M1. Moreover, it is

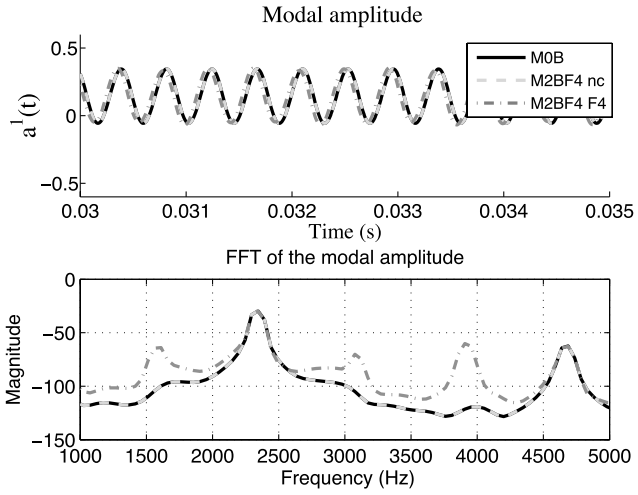

a) Model M2BF4

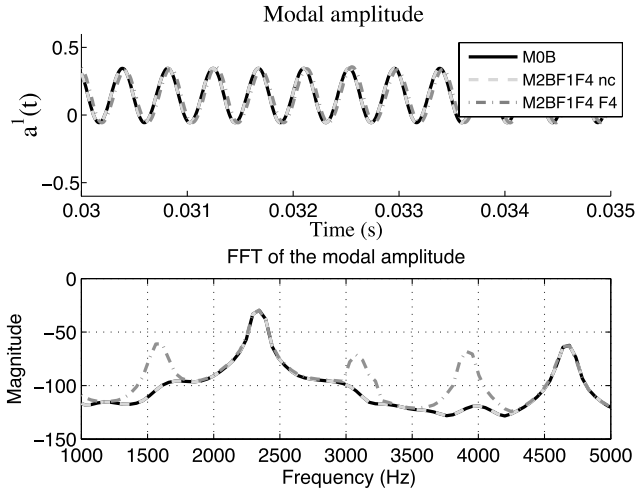

b) Model M2BF1F4

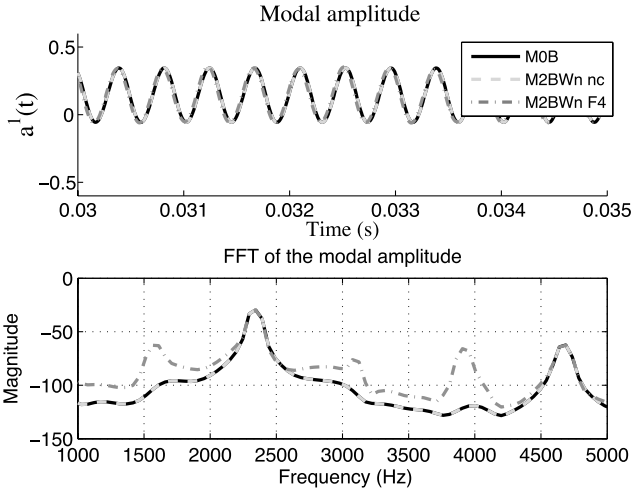

c) Model M2Wn

Fig. 10 Time series and power spectrum of the first modal amplitude of the Galerkin system obtained using method M2. Results for the baseline model M0B are reported for comparison.

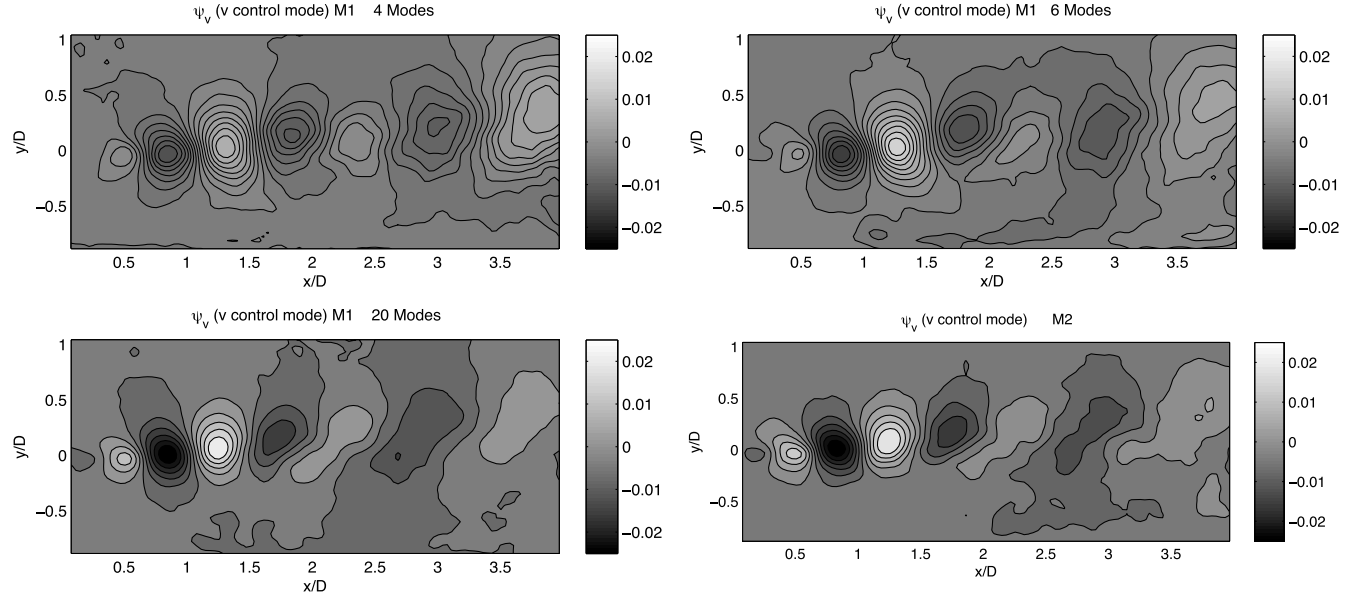

Fig. 11 Comparison between the actuated POD-stochastic estimation (M1) and the $\mathcal{L}_2$ optimization (M2) methods.

Table 1 Nomenclature for baseline and open-loop forced flows and models

Case	Comments
B	Baseline flow
F1	Open-loop forcing at $f = 1610$ Hz
F4	Open-loop forcing at $f = 3920$ Hz
Wn	Band-limited white noise forcing
M0	Subdomain separation method
M0B	Model based on method M0 using baseline snapshots
M0BF4	Model based on method M0 using baseline and F4 snapshots
M0BF1F4	Model based on method M0 using baseline, F1, and F4 snapshots
M0BWn	Model based on method M0 using Wn snapshots
M1	Separation method using actuated POD expansion
M1BF4	Model based on method M1 using baseline and F4 snapshots
M1BF1F4	Model based on method M1 using baseline, F1, and F4 snapshots
M1BWn	Model based on method M1 using baseline and Wn snapshots
M2	Separation method using $\mathcal{L}_2$ optimization
M2BF4	Model based on method M2 using baseline and F4 snapshots
M2BF1F4	Model based on method M2 using baseline, F1, and F4 snapshots
M2BWn	Model based on method M2 using baseline and Wn snapshots

Table 2 Comparison criteria for the subdomain (M0), actuated POD-stochastic estimation (M1), and $\mathcal{L}_2$ optimization (M2) methods

Criteria	M0	M1	M2
Provides the input Γ as a separate term	Yes	Yes	Yes
Requires identification of a control region	Yes	No	No
Consistent with baseline flow for $\Gamma = 0$	No	Yes	Yes
Correctly estimates magnitudes of control terms	No	Yes	Yes

also reasonable to expect that, as the number of actuated POD modes increases, the result of the actuated POD method with linear stochastic estimation approaches that of the $\mathcal{L}_2$ optimization, that is,

$$\lim_{N_{\mathrm{ac}}\to\infty} \sum_{i=1}^{N_{\mathrm{ac}}} M_i \phi_i^{\mathrm{ac}} = \psi^*$$

This intuition is supported by the results shown in Fig. 11, which compares the optimal mode found by $\mathcal{L}_2$ optimization with the modes ψ_1 resulting from the method M1 with linear stochastic estimation when $N_{\mathrm{ac}} = 4$, 6, and 20, respectively. For reasons of space, only the modes associated with the vertical components of the velocity are shown. Comparing the figures, it is seen that, indeed, this conjecture seems to be verified.

Although M2 is undoubtedly a more economical method than M1 (no stochastic estimation is required, hence it is less expensive from a

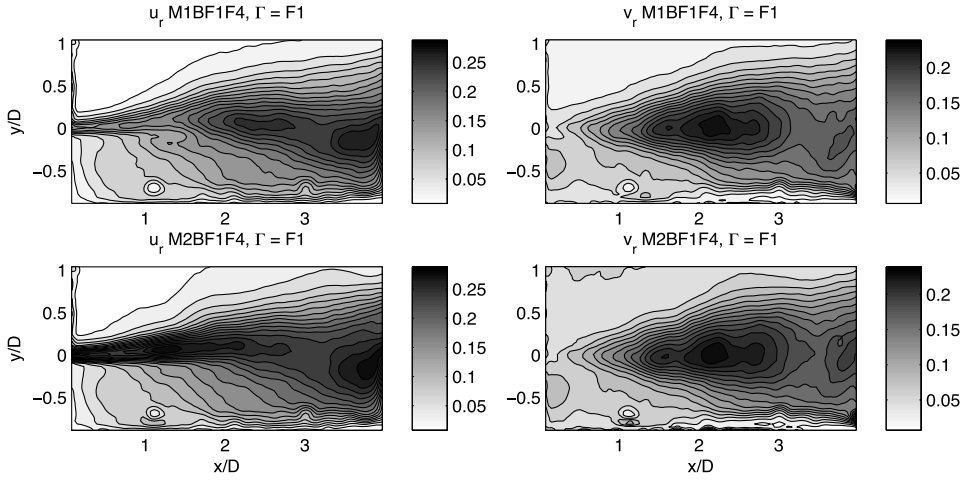

a) Actuation modes based on combination of F1 and F4 forcing

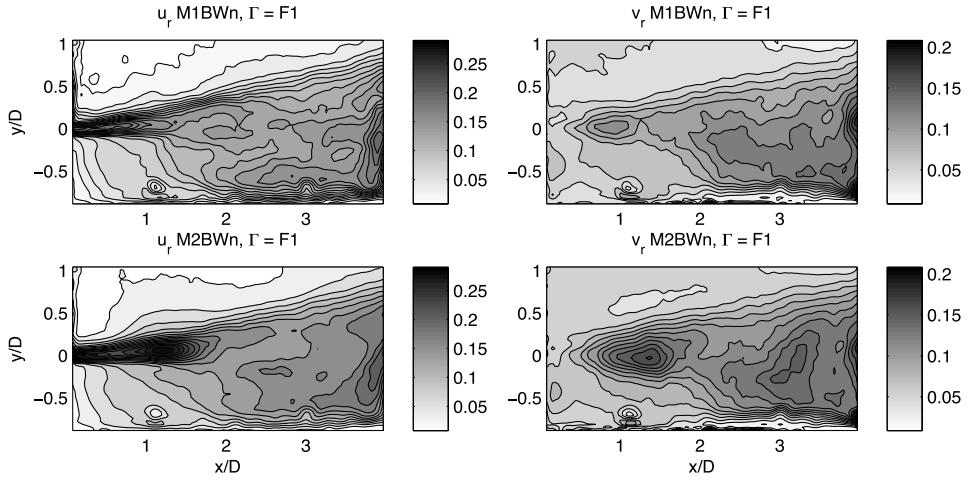

b) Actuation modes based on white noise forcing

Fig. 12 Mean-squared error in the reconstruction of the velocity field for forced case F1. Actuation modes based on a) combination of F1 and F4 forcing, and b) white noise forcing.

computational point of view), the M1 approach offers more flexibility, in the sense that no particular dependence is assumed a priori between the input and the temporal coefficients $a_i^{ac}(t)$ of the actuation modes ϕ_i^{ac} in the augmented POD expansion. This, in turn, leaves an additional degree of freedom to be exploited for the design of the estimator, which is not limited a priori to a linear least-squares algorithm. In synthesis, it is fair to say that although method M2 offers a preferable solution over method M1 when a very-low-order and low-complexity model is sought, method M1 is more general, and may lead to better results in specific applications.

Finally, Table 2 shows a summary of the benefits of the M1 and M2 methods for reduced-order modeling as compared with the subdomain separation method. For the new separation methods, the PIV images used to obtain the POD modes do not require an identifiable control input region. Therefore, method M1 or M2 can be used in the study of flowfields where it is difficult to capture the control input region or where the region of interest is away from the boundaries where the control is applied. Unlike M0, methods M1 and M2 reduce exactly to the baseline case under no input ($\Gamma = 0$) condition and improve the scaling of the control-related terms in the reduced-order models. In particular, it has been verified (see next section) that reduced-order model-based controllers designed on the basis of either M1 or M2 can be applied to real-time experiments without the need to resort to substantial ad hoc modifications of the controller gains.

V. Model Validation and Experimental Results

This section will provide experimental results to test the behavior of reduced-order models based on the two new methods, derived using combinations of snapshots of various forced flow conditions. The performance of the new models will be also compared with the best case obtained for the subdomain separation method in previous studies. The models will be evaluated in their capability to yield a reconstruction of snapshots of actuated flow velocity fields (in open-loop operation), as well in their capability to provide reduced-order models which are suitable for model-based control (in closed-loop operation).

A. Velocity Reconstruction

The first test to evaluate the quality of the new models concerns the reconstruction of the velocity field of individual forced cases using the baseline POD expansions augmented with the actuation modes. Snapshots of the reconstructed flowfield will be compared with snapshots of the original flowfield to evaluate the ability of the

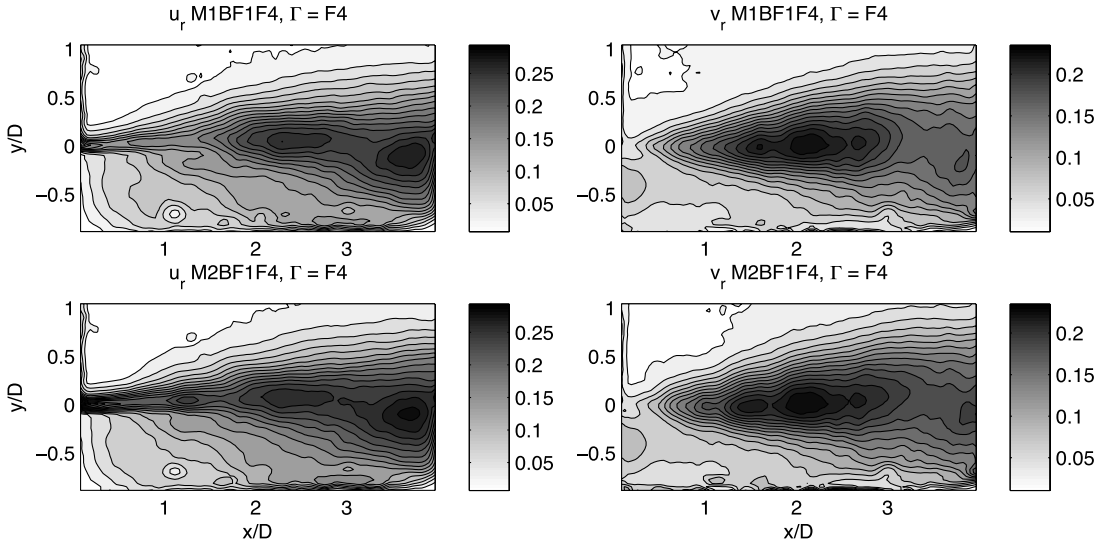

a) Actuation modes based on combination of F1 and F4 forcing

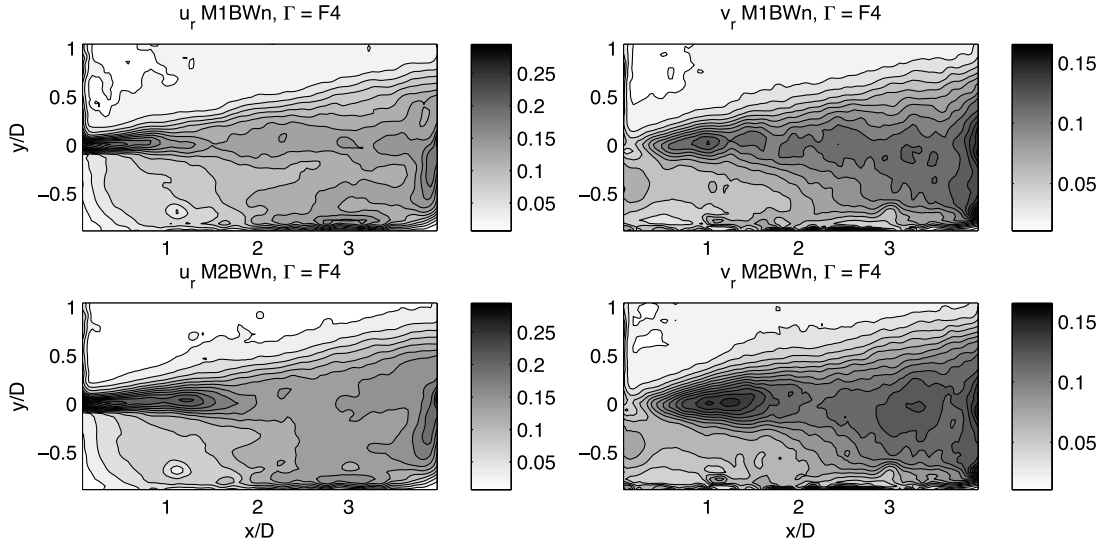

b) Actuation modes based on white noise forcing

Fig. 13 Mean-squared error in the reconstruction of the velocity field for forced case F4. Actuation modes based on a) combination of F1 and F4 forcing, and b) white noise forcing.

models to recover various forced flow cases. This will allow us to confirm that the newly developed techniques perform satisfactorily at the POD expansion level, before Galerkin projection is applied. Also, this test will be used to determine the most appropriate selection of the forcing condition to be employed in the construction of the POD basis, which is one of the outstanding problems in reduced-order modeling.

Models for methods M1 and M2 have been obtained using snapshots of individual forced flows (namely, F4 or Wn) and combination of the forced case F1 and F4. The snapshots used for the construction of the actuation modes will be referred to as the model identification data set, and those used for evaluation as the model validation data set. The nomenclature used to identify the models is summarized in Table 1.

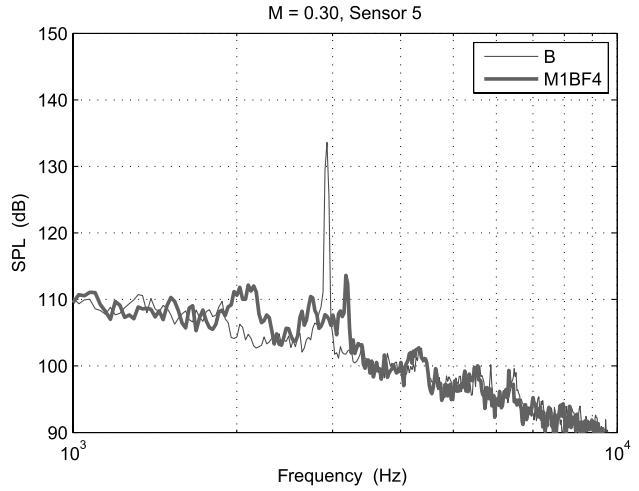

a) Model M1BF4

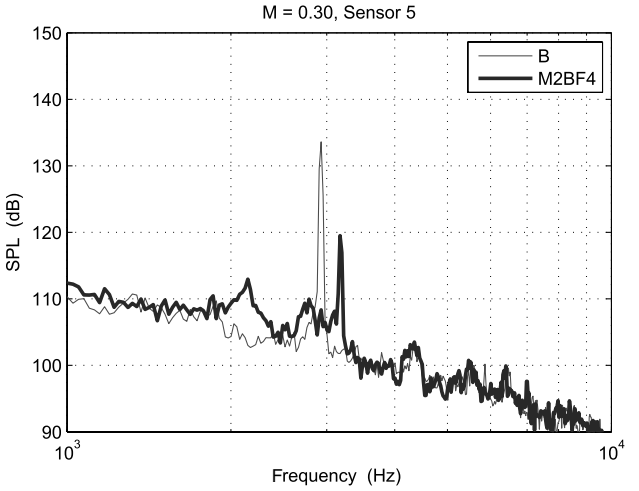

b) Model M2BF4

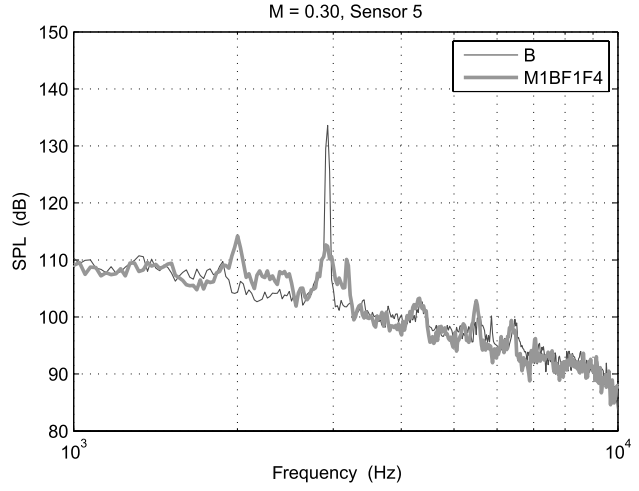

c) Model M1BF1F4

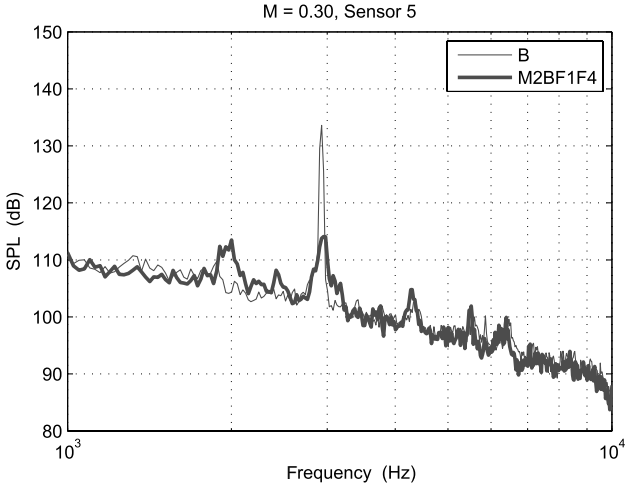

d) Model M2BF1F4

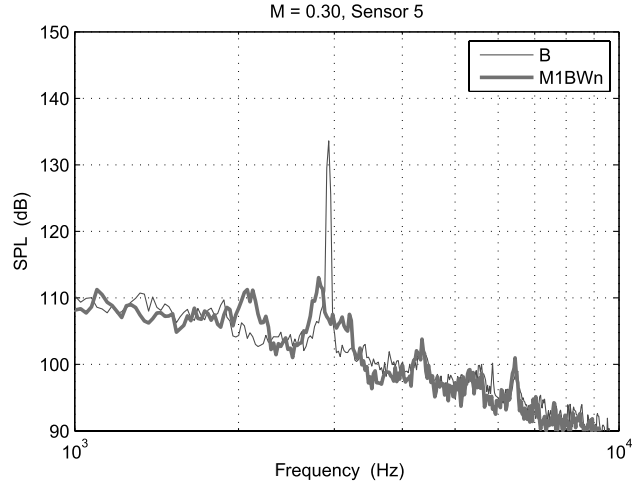

e) Model M1Bwn

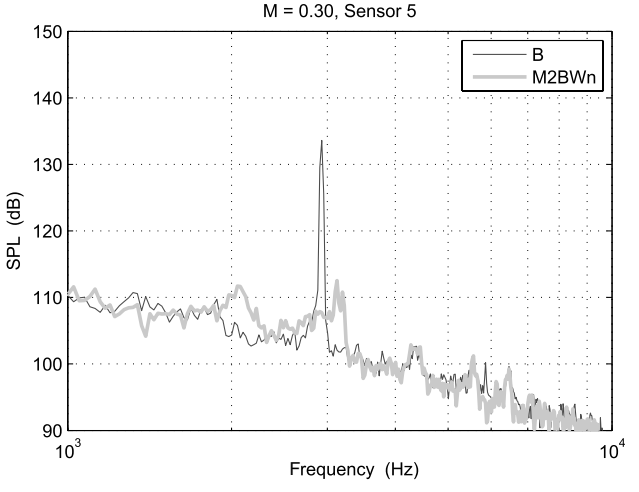

f) Model M2BWn

Fig. 14 Sound pressure level obtained under LQ control at design condition $M = 0.30$, for models built with methods M1 (left) and M2 (right).

For the reconstruction of the velocity field, first, the baseline modes and the actuation modes are computed using the identification data specific to a given model. It must be noted that the average value of the augmented velocity field $\boldsymbol{q}_0(\boldsymbol{x})$ is computed at this stage using baseline snapshots only, because it has been shown in Little et al. [40] that, for the current flow conditions, the external forcing does not substantially affect the mean flow. Then, for the model validation data $(\boldsymbol{q}(\boldsymbol{x}, t_k), \Gamma(t_k))$, the reconstructed flowfield is obtained by projecting the velocity fluctuations onto the baseline basis and by multiplying the control modes by the corresponding value of the input Γ, measured at the same time the PIV image is acquired. For instance, for the M1 method, this corresponds to computing the reconstructed flowfield fluctuation $\boldsymbol{q}_r(x, t)$ as

$$\boldsymbol{q}_r(\boldsymbol{x}, t_k) = \sum_{i=1}^{N} \left\langle \boldsymbol{q}(\boldsymbol{x}, t_k), \phi_i^b(\boldsymbol{x}) \right\rangle \phi_i^b(\boldsymbol{x}) + \Gamma(t_k)\psi_1(\boldsymbol{x}) + \Gamma(t_k)^2\psi_2(\boldsymbol{x})$$

and similarly for M2. Then, the mean-squared error between the actual velocity and its reconstructed value is computed as follows:

$$\boldsymbol{e}(\boldsymbol{x}) = \sqrt{\frac{1}{N_s}\sum_{k=1}^{N_s}[\boldsymbol{q}_r(\boldsymbol{x}, t_k) - \boldsymbol{q}(\boldsymbol{x}, t_k)]^2} \tag{14}$$

where N_s is the number of snapshots in the model validation data set.

The most interesting cases, which will be discussed here, regard, respectively, the following situations:

1) The identification data set includes snapshots of the forcing condition used for validation, together with snapshots from other forced flows.

2) Model identification has been carried out using flow forced with band-limited white noise.

As a matter of fact, it is well known that using the same data set for both model identification and model validation does not constitute a statistically reliable test. On the other hand, a sizable approximation error is somewhat expected when using completely different data sets (for example, F1 for identification and F4 for validation).

The results shown here correspond to the cases when the F1–F4 and the Wn control modes are used to reconstruct the forced cases F1 (Fig. 12) and F4 (Fig. 13). The figures show the mean-square error in each velocity component for both separation methods, M1 and M2. Surprisingly enough, it is clear from both figures that the error levels are lower for the Wn-based modes (Figs. 12b and 13b). In this case, the error is concentrated in the initial shear layer region and close to the leading edge. We suspect that this is due to two factors: 1) the difference in mean flow, which has been neglected in the modeling, and 2) existence of smaller-scale structures and larger gradients in the initial shear layer region, which could contribute to both measurement and calculation errors. For the results based on identification data F1–F4, it can be observed that the error spreads in a larger region, midway point in the cavity, and toward the trailing edge. We believe that the main reason for the difference in the mean error is the nature of the structures present in the control mode basis. It can be noticed in Figs. 7 and 9 that the actuation modes for the F1–F4 case contain large and well-organized structures, whereas the Wn case does not. The structures arise as a result of the periodic forcing used in the F1–F4 case, which tends to bias the data. Reconstruction using the F1 or F4 basis for identification showed a behavior similar to the F1–F4 case, with lower error levels for the same forcing used for validation and higher for the other. However, the Wn case still showed the best results among all the cases tested.

B. Feedback Control

The next step is to compare the performance of feedback controllers built on the basis of the given models. As discussed in the Introduction, our group at GDTL has already obtained satisfactory experimental results in closed-loop operation with a controller designed on the basis of reduced-order models relying upon the initial method M0 [20]. The aim of the comparison between M1 and M2 to M0 in this section is to verify that controller designs using the new models perform at least as well as the previous one in experiments, if not better.

The feedback control algorithm for the new models was designed using the scaled linear quadratic (LQ) approach that was adopted in our previous studies [20,45]. The controllers obtained for the new models M1BF4, M2BF4, M1BF1F4, M2BF1F4, M1BWn, and M2BWn are tested experimentally in the cavity flow and the results are compared with those obtained with the initial model MB0. Figure 14 shows the SPL reduction obtained by the LQ state feedback control for the different models tested in Mach 0.3 cavity flow, which is the design condition. The thin line yields the SPL of the unforced baseline flow, whereas the thick line corresponds to the SPL of the flow at the same location under state feedback control. It can be observed from the figure that all the models show improvement with respect to the uncontrolled flow by reducing the resonant peak by more than 18 dB. However the controllers based on M1BF4 and M2BF4 seem to exacerbate a peak around 3.2 kHz, near the resonance frequency, although this behavior is not observed for the other controllers. Overall, the results compare very favorably with those obtained with the model MB0, shown in Fig. 15. As we have done in our previous studies for the initial method (M0), the performance of the controllers are also tested in closed-loop experiments for off-design flow conditions in the neighborhood of Mach 0.30. As an example, Fig. 16 shows the performance of the closed-loop system for a Mach 0.28 flow. It can be noticed that each controller is capable of maintaining qualitatively the same general characteristics and benefits as in the Mach 0.30 design condition. This is consistent with our previous results [20], which showed the robustness of the control-loop system for small deviations from the design condition. Finally, to quantify the benefits of each model, the average reduction obtained in the overall sound pressure level (OASPL) vs the mean voltage (Vrms) used for each controller have been computed and compared. Whereas the results presented in Figs. 15 and 16 are based on a single pressure sensor, the OASPL results are based on all six sensors used in the experiments (see Fig. 2b). Figure 17 shows the result of this comparison for all the different models used in each of the two freestream flow conditions tested. An important observation is that the models based on the new separation methods require less power to achieve similar or better performance. This is true for all the flows tested. Overall, the models based on white noise identification data perform significantly better than the others, especially as far as model M1BWn is concerned. This is a clear indication that a better representation of the flow dynamics is attained in this case, and thus the corresponding controller tends to operate closer to optimal conditions.

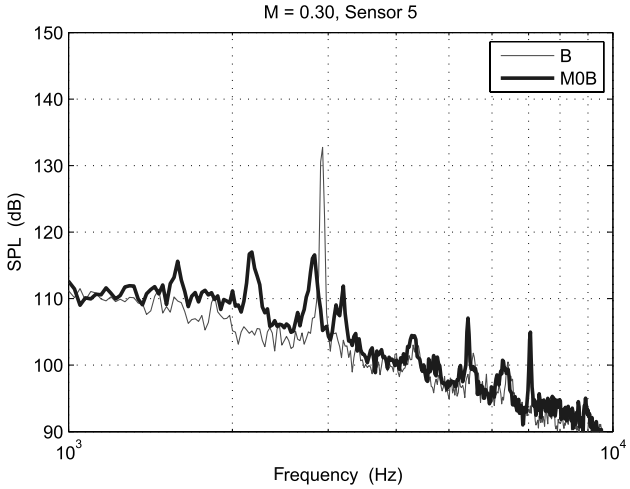

Fig. 15 Sound pressure level obtained under LQ control at design condition $M = 0.30$, for model built with method M0 (Samimy et al. [20]).

VI. Conclusions

In this paper, we presented our most recent progress in the development of reduced-order model-based feedback flow control. Two new control input separation methods are developed and tested experimentally. The methods incorporate the control input through an additional set of modes obtained from the innovation between a forced flow and its projection onto the baseline modes. The new methods are developed to address the issues and restrictions raised about the initial subdomain separation method, especially from the theoretical point of view. Toward this goal, the new models provided important improvements over the initial methodology. The new methods were then evaluated at the POD level for their ability to reconstruct different actuated flows, even those that are not part of the data set used for model identification. It was observed that the best performance in terms of reconstruction of a wide range of flows were obtained for models built from the basis obtained from white noise

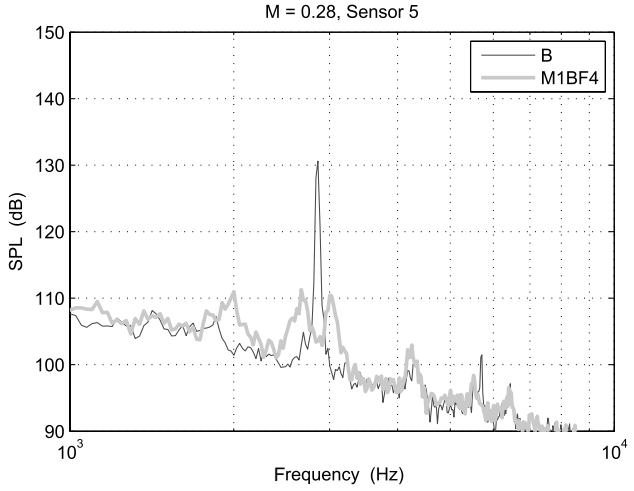

a) Model M1BF4

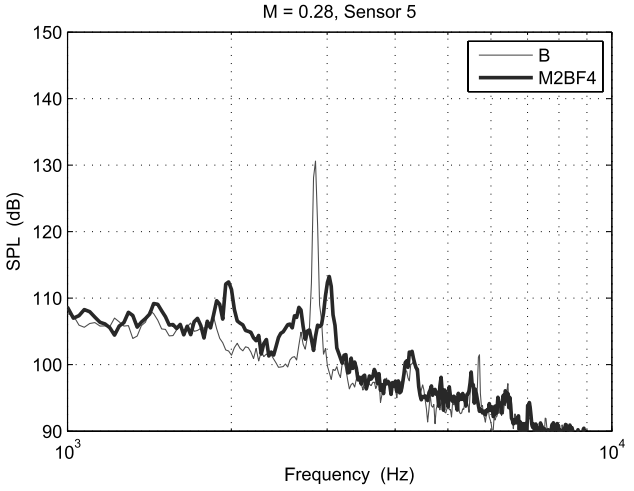

b) Model M2BF4

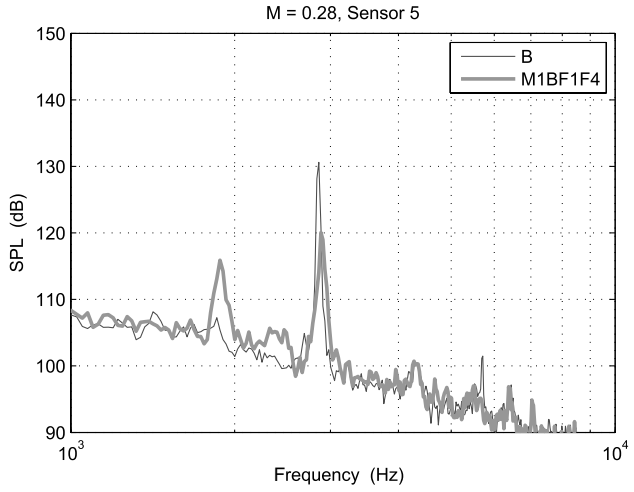

c) Model M1BF1F4

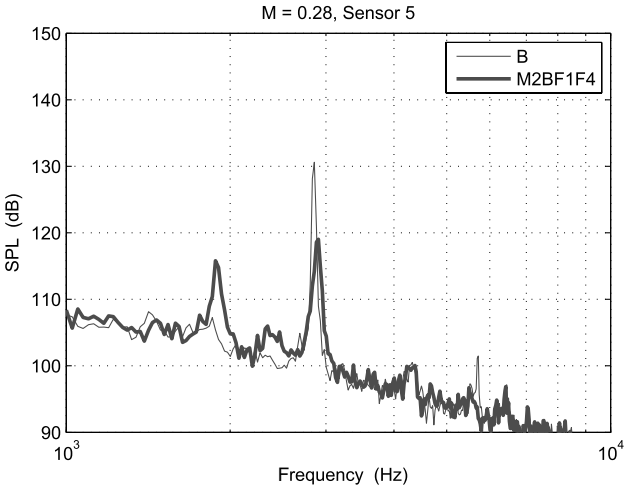

d) Model M2BF1F4

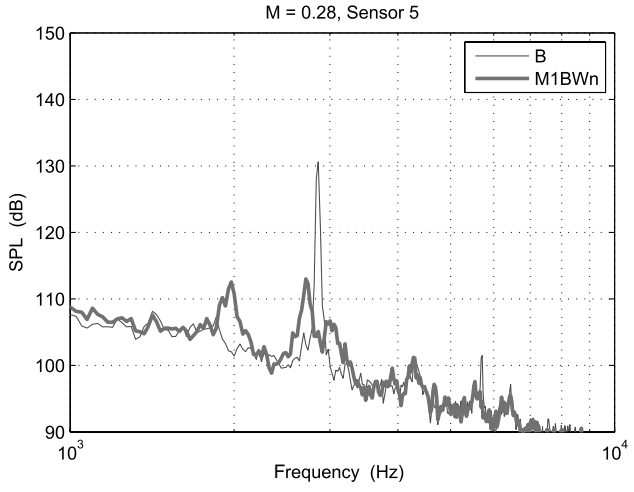

e) Model M1BWn

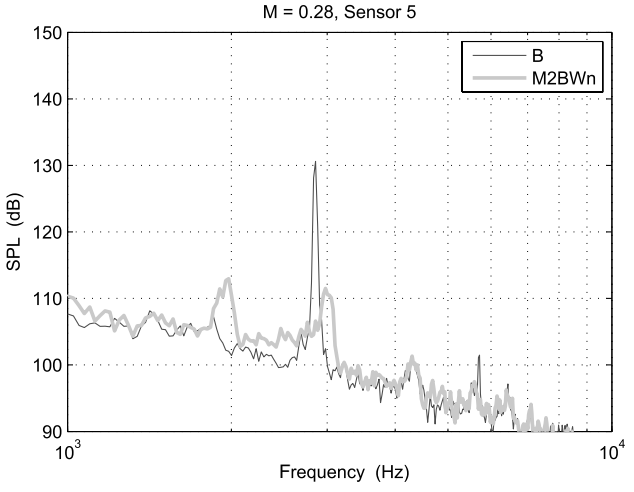

f) Model M2BWn

Fig. 16 SPL under LQ control at off-design condition $M = 0.28$, for models built with methods M1 (left) and M2 (right).

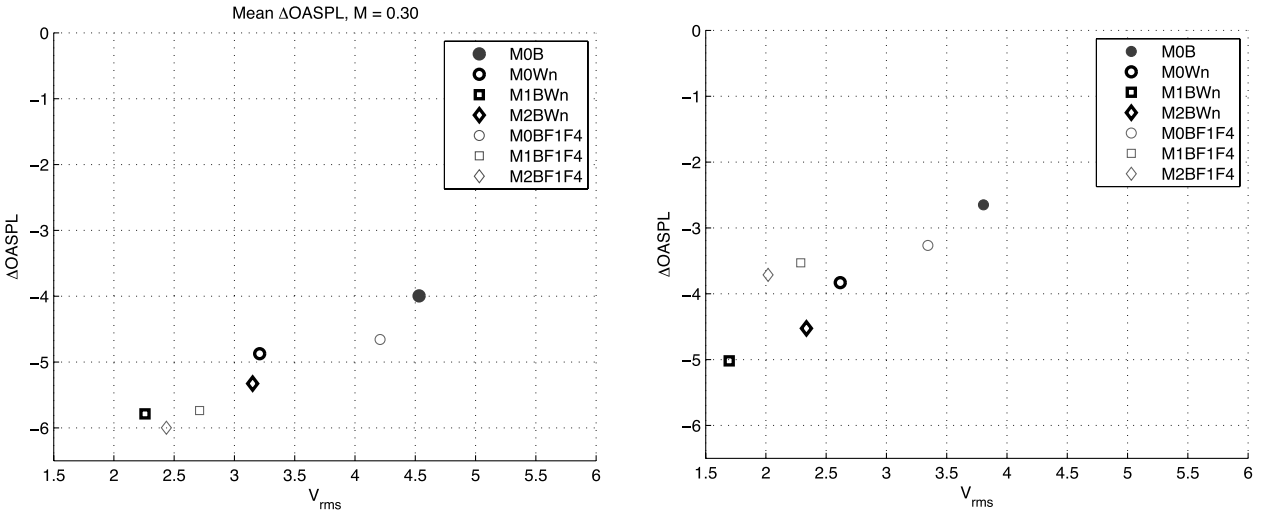

a) $M = 0.30$ **b) $M = 0.28$**

Fig. 17 Root mean square voltage vs average OASPL for several models at different Mach numbers: a) $M = 0.3$ (design condition), b) $M = 0.28$ (off-design condition).

excitation. Linear-quadratic controllers, built on the basis of the models obtained from the new separation methods, were tested in experiments. The results obtained showed that all the controllers significantly reduce the resonant peak of the single-mode Mach 0.3 flow, for which they were designed, without significantly introducing other undesirable peaks. The controllers also performed satisfactorily for off-design conditions. These results compared favorably or behaved similarly to the controllers designed in our previous studies. However, the new models showed a distinct superiority in terms of the ratio between overall sound pressure level attenuation and power consumption. Finally, the analysis revealed that models derived using white noise forcing outperform the others. Although the results are preliminary, the possible outcome is quite appealing: Applying white noise forcing does not require one to evaluate the system response under forcing to select the frequencies that yield the desired response. This reduces the amount of experimental data required and the runtime for the modeling process, and could constitute a possible answer to the long-standing question regarding which flow conditions to use in the identification of reduced-order models.

Appendix A: Governing Equations

The nondimensional** isentropic compressible Navier–Stokes equations given in Eq. (1) can be expressed in compact form as follows [41]:

$$\dot{\bar{\boldsymbol{q}}} = \frac{1}{Re}\boldsymbol{L}_1(\bar{\boldsymbol{q}}) + \frac{1}{M^2}\boldsymbol{Q}_1(\bar{\boldsymbol{q}},\bar{\boldsymbol{q}}) + \boldsymbol{Q}_2(\bar{\boldsymbol{q}},\bar{\boldsymbol{q}}) \tag{A1}$$

where $\bar{\boldsymbol{q}} = (u, v, c) = \boldsymbol{q} + \boldsymbol{q}_0$ denotes the augmented flow velocity, and

$$\boldsymbol{L}_1(\bar{\boldsymbol{q}}) = \begin{pmatrix} u_{xx} + v_{yy} \\ v_{xx} + v_{yy} \\ 0 \end{pmatrix}, \qquad \boldsymbol{Q}_1(\bar{\boldsymbol{q}}_1,\bar{\boldsymbol{q}}_2) = \frac{2}{\kappa - 1}\begin{pmatrix} c_1 c_{2x} \\ c_1 c_{2y} \\ 0 \end{pmatrix}$$

$$\boldsymbol{Q}_2(\bar{\boldsymbol{q}}_1,\bar{\boldsymbol{q}}_2) = \begin{pmatrix} u_1 u_{2x} + v_1 u_{2y} \\ u_1 v_{2x} + v_1 v_{2y} \\ u_1 c_{2x} + v_1 c_{2y} + \frac{\kappa-1}{2} c_1 (u_{2x} + v_{2y}) \end{pmatrix}$$

Since $\dot{\boldsymbol{q}}_0 = 0$, Eq. (A1) yields

$$\begin{aligned}
\dot{\boldsymbol{q}} &= \frac{1}{Re}\boldsymbol{L}_1(\boldsymbol{q} + \boldsymbol{q}_0) + \frac{1}{M^2}\boldsymbol{Q}_1(\bar{\boldsymbol{q}} + \boldsymbol{q}_0, \bar{\boldsymbol{q}} + \boldsymbol{q}_0) \\
&\quad + \boldsymbol{Q}_2(\bar{\boldsymbol{q}} + \boldsymbol{q}_0, \bar{\boldsymbol{q}} + \boldsymbol{q}_0) = \frac{1}{Re}\boldsymbol{L}_1(\boldsymbol{q}_0) + \frac{1}{Re}\boldsymbol{L}_1(\boldsymbol{q}) \\
&\quad + \frac{1}{M^2}\boldsymbol{Q}_1(\boldsymbol{q}_0,\boldsymbol{q}_0) + \frac{1}{M^2}\boldsymbol{Q}_1(\boldsymbol{q}_0,\boldsymbol{q}) + \frac{1}{M^2}\boldsymbol{Q}_1(\boldsymbol{q},\boldsymbol{q}_0) \\
&\quad + \frac{1}{M^2}\boldsymbol{Q}_1(\boldsymbol{q},\boldsymbol{q}) + \boldsymbol{Q}_2(\boldsymbol{q}_0,\boldsymbol{q}_0) + \boldsymbol{Q}_2(\boldsymbol{q}_0,\boldsymbol{q}) \\
&\quad + \boldsymbol{Q}_2(\boldsymbol{q},\boldsymbol{q}_0) + \boldsymbol{Q}_2(\boldsymbol{q},\boldsymbol{q})
\end{aligned}$$

Therefore, Eq. (2) holds with

$$\begin{aligned}
\boldsymbol{C} &= \frac{1}{Re}\boldsymbol{L}(\boldsymbol{q}_0) + \frac{1}{M^2}\boldsymbol{Q}_1(\boldsymbol{q}_0,\boldsymbol{q}_0) + \boldsymbol{Q}_2(\boldsymbol{q}_0,\boldsymbol{q}_0) \\
\boldsymbol{L}(\boldsymbol{q}) &= \frac{1}{Re}\boldsymbol{L}(\boldsymbol{q}) + \frac{1}{M^2}\boldsymbol{Q}_1(\boldsymbol{q}_0,\boldsymbol{q}) + \frac{1}{M^2}\boldsymbol{Q}_1(\boldsymbol{q},\boldsymbol{q}_0) \\
&\quad + \boldsymbol{Q}_2(\boldsymbol{q}_0,\boldsymbol{q}) + \boldsymbol{Q}_2(\boldsymbol{q},\boldsymbol{q}_0) \\
\boldsymbol{Q}(\boldsymbol{q},\boldsymbol{q}) &= \frac{1}{M^2}\boldsymbol{Q}_1(\boldsymbol{q},\boldsymbol{q}) + \boldsymbol{Q}_2(\boldsymbol{q},\boldsymbol{q})
\end{aligned}$$

Appendix B: Proof of Theorem IV.1

1) Note that

$$J(\psi) = E\{\|\tilde{\boldsymbol{q}}_k\|^2 - 2\Gamma_k\langle\tilde{\boldsymbol{q}}_k, \psi\rangle + (\Gamma_k)^2\|\psi\|^2\}$$

Since J is quadratic in ψ with positive leading coefficient $E\{\Gamma_k^2\}$, it has a unique minimum. Computing the first variation of J with respect to $\boldsymbol{\xi} \in \mathbb{H}$ yields

$$\begin{aligned}
\frac{\mathrm{d}}{\mathrm{d}\delta}\bigg|_{\delta=0} J(\psi + \delta\boldsymbol{\xi}) &= \frac{\mathrm{d}}{\mathrm{d}\delta}\bigg|_{\delta=0} E\{\|\tilde{\boldsymbol{q}}_k\|^2 - 2\Gamma_k\langle\tilde{\boldsymbol{q}}_k, \psi + \delta\boldsymbol{\xi}\rangle \\
&\quad + \Gamma_k^2 \parallel \psi + \delta\boldsymbol{\xi}\|^2\} = E\{-2\Gamma_k\langle\tilde{u}_k, \boldsymbol{\xi}\rangle + \Gamma_k^2\langle\psi + \delta\boldsymbol{\xi}, \boldsymbol{\xi}\rangle \\
&\quad + \Gamma_k^2\langle\boldsymbol{\xi}, \psi + \delta\boldsymbol{\xi}\rangle\}|_{\delta=0} = E\Big\{\Big\langle -2\Gamma_k\tilde{\boldsymbol{q}}_k + 2\Gamma_k^2\psi, \boldsymbol{\xi}\Big\rangle\Big\} \\
&= \Big\langle E\Big\{-2\Gamma_k\tilde{\boldsymbol{q}}_k + 2\Gamma_k^2\psi\Big\}, \boldsymbol{\xi}\Big\rangle
\end{aligned}$$

For ψ to be an extremum of J, its first variation must vanish $\forall\ \boldsymbol{\xi} \in \mathbb{H}$. Therefore,

$$E\Big\{-2\Gamma_k\tilde{\boldsymbol{q}}_k + 2\Gamma_k^2\psi^*\Big\} = 0$$

**The governing equations have been nondimensionalized by scaling $\boldsymbol{u}$ by the freestream velocity U_∞, the local speed of sound by the ambient sound speed $c_\infty = (\kappa R T_\infty)^{1/2}$, where T_∞ is the ambient temperature, the Cartesian coordinates $\boldsymbol{x}$ by the cavity depth D, time by D/U_∞, and pressure by $\bar{\rho}U_\infty^2$, where $\bar{\rho}$ denotes mean density.

and thus, by linearity of $E\{\cdot\}$,

$$\psi^* = \frac{E\{\Gamma_k \tilde{\boldsymbol{q}}_k\}}{E\{\Gamma_k^2\}}$$

2) The fact that $\psi^* \in \mathbb{H}$ follows immediately from linearity of $E\{\cdot\}$.

3) To show that $\psi^* \perp \phi_i^b$ for $i = 1, \ldots, N$, first note that $\tilde{\boldsymbol{q}}_k \perp S$. Then, for any $i = 1, \ldots, N$

$$\langle \psi^*, \phi_i^b \rangle = \left\langle \frac{E\{\Gamma_k \tilde{\boldsymbol{q}}_k\}}{E\{\Gamma_k^2\}}, \phi_i^b \right\rangle = \frac{E\{\Gamma_k \langle \tilde{\boldsymbol{q}}_k, \phi_i^b \rangle\}}{E\{\Gamma_k^2\}} = \frac{E\{0\}}{E\{\Gamma_k^2\}} = 0$$

Acknowledgments

This work has been supported by the U.S. Air Force Research Laboratory/Air Vehicles Directorate and U.S. Air Force Office of Scientific Research through the Collaborative Center of Control Science (Contract F33615-01-2-3154). The authors would like to thank their colleagues at the Collaborative Center of Control Science, James Myatt, Chris Camphouse, Marco Debiasi, Kihwan Kim, and Jesse Little for assistance and fruitful discussions. The use of the actuated proper orthogonal decomposition expansion was originally suggested by Dietmar Rempfer.

References

[1] Bensoussan, A., Prato, D. D., Delfour, M. C., and Mitter, S. K., *Representation and Control of Infinite Dimensional Systems*, Birkhauser, Boston, 1992.

[2] Gad-el-Hak, M., *Flow Control: Passive, Active, and Reactive Flow Management*, Cambridge Univ. Press, New York, 2000.

[3] Aamo, O. M., and Krstic, M., *Flow Control by Feedback: Stabilization and Mixing*, Springer, New York, 2003.

[4] King, R. (ed.), *Active Flow Control*, Vol. 95, Notes on Numerical Fluid Mechanics and Multidisciplinary Design, Springer, Berlin, 2007.

[5] Kook, H., Mongeau, L., and Franchek, M. A., "Active Control of Pressure Fluctuations Due to Flow Over Helmholtz Resonators," *Journal of Sound and Vibration*, Vol. 255, No. 1, Aug. 2002, pp. 61–76. doi:10.1006/jsvi.2001.4149

[6] Cabell, R. H., Kegerise, M. A., Cox, D. E., and Gibbs, G. P., "Experimental Feedback Control of Flow Induced Cavity Tones," AIAA Paper 2002-2497, June 2002.

[7] Kegerise, M. A., Cattafesta, L. N., and Ha, C., "Adaptive Identification and Control of Flow-Induced Cavity Oscillations," AIAA Paper 2002-3158, June 2002.

[8] Glauser, M., Eaton, E., Taylor, J., Cole, D., Ukeiley, L., Citriniti, J., George, W., and Stokes, S., "Low-Dimensional Descriptions of Turbulent Flows: Experiment and Modeling," AIAA Paper 1999-3699, June 1999.

[9] Rempfer, D., "On Low-Dimensional Galerkin Models for Fluid Flow," *Theoretical and Computational Fluid Dynamics*, Vol. 14, No. 2, June 2000, pp. 75–88. doi:10.1007/s001620050131

[10] Delville, J., Ukeiley, L., Cordier, L., Bonnet, J. P., and Glauser, M., "Examination of Large-Scale Structures in a Turbulent Plane Mixing Layer, 1: Proper Orthogonal Decomposition," *Journal of Fluid Mechanics*, Vol. 391, July 1999, pp. 91–122. doi:10.1017/S0022112099005200

[11] Ukeiley, L., Cordier, L., Manceau, R., Delville, J., Glauser, M., and Bonnet, J. P., "Examination of Large-Scale Structures in a Turbulent Plane Mixing Layer, 2: Dynamical Systems Model," *Journal of Fluid Mechanics*, Vol. 441, Aug. 2001, pp. 67–108. doi:10.1017/S0022112001004803

[12] Noack, B. R., Afanasiev, K., Morzynski, M., Tadmor, G., and Thiele, F., "Hierarchy of Low-Dimensional Models for the Transient and Post-Transient Cylinder Wake," *Journal of Fluid Mechanics*, Vol. 497, Dec. 2003, pp. 335–363. doi:10.1017/S0022112003006694

[13] Rowley, C. W., Williams, D. R., Colonius, T., Murray, R. M., and Macmynowski, D. G., "Linear Models for Control of Cavity Flow Oscillations," *Journal of Fluid Mechanics*, Vol. 547, Jan. 2006, pp. 317–330. doi:10.1017/S0022112005007299

[14] Holmes, P., Lumley, J., and Berkooz, G., *Turbulence, Coherent Structures, Dynamical System, and Symmetry*, Cambridge Univ. Press, Cambridge, England, U.K., 1996.

[15] Berkooz, G., Holmes, P., and Lumley, J. L., "Proper Orthogonal Decomposition in the Analysis of Turbulent Flows," *Annual Review of Fluid Mechanics*, Vol. 25, Jan. 1993, pp. 539–575. doi:10.1146/annurev.fl.25.010193.002543

[16] Gillies, E., "Low-Dimensional Control of the Circular Cylinder Wake," *Journal of Fluid Mechanics*, Vol. 371, Sept. 1998, pp. 157–178. doi:10.1017/S0022112098002122

[17] Noack, B., Tadmor, G., and Morzynski, M., "Low-Dimensional Models for Feedback Flow Control, Part 1: Empirical Galerkin Models," AIAA Paper 2004-2408, June 2004.

[18] Tadmor, G., Noack, B., Morzynski, M., and Siegel, S., "Low-Dimensional Models for Feedback Flow Control, Part 2: Controller Design and Dynamic Estimation," AIAA Paper 2004-2409, June 2004.

[19] Siegel, S. G., Cohen, K., and McLaughlin, T., "Numerical Simulations of a Feedback-Controlled Circular Cylinder Wake," *AIAA Journal*, Vol. 44, No. 6, June 2006, pp. 1266–1276. doi:10.2514/1.4443

[20] Samimy, M., Debiasi, M., Caraballo, E., Serrani, A., Yuan, X., Little, J., and Myatt, J., "Feedback Control of Subsonic Cavity Flows Using Reduced-Order Models," *Journal of Fluid Mechanics*, Vol. 579, May 2007, pp. 315–346. doi:10.1017/S0022112007005204

[21] Hogberg, M., Bewley, T. R., and Henningson, D. S., "Linear Feedback Control and Estimation of Transition in Plane Channel Flow," *Journal of Fluid Mechanics*, Vol. 481, April 2003, pp. 149–175. doi:10.1017/S0022112003003823

[22] Camphouse, R. C., "Boundary Feedback Control Using Proper Orthogonal Decomposition Models," *Journal of Guidance, Control, and Dynamics*, Vol. 28, Sept.–Oct. 2005, pp. 931–938. doi:10.2514/1.10523

[23] Fitzpatrick, K., Feng, Y., Lind, R., Kurdila, A. J., and Mikolaitis, D. W., "Flow Control in a Driven Cavity Incorporating Excitation Phase Differential," *Journal of Guidance, Control, and Dynamics*, Vol. 28, No. 1, 2005, pp. 63–70. doi:10.2514/1.4664

[24] Lawrence, D., Myatt, J., and Camphouse, R., "On Model Reduction via Empirical Balanced Truncation," *Proceedings of the 2005 American Control Conference*, American Automatic Control Council, Evanston, IL, June 2005, pp. 3139–3144.

[25] Gunzburger, M., "Adjoint Equation-Based Methods for Control Problems in Incompressible, Viscous Flows," *Flow, Turbulence and Combustion*, Vol. 65, Nos. 3–4, 2000, pp. 249–272. doi:10.1023/A:1011455900396

[26] Cohen, K., Siegel, S., Seidel, J., and McLaughlin, T., "Neural Network Estimator for Low-Dimensional Modeling of a Cylinder Wake," AIAA Paper 2006-3491, June 2006.

[27] Cohen, K., Siegel, S., McLaughlin, T., and Gillies, E., "Feedback Control of a Cylinder Wake Low-Dimensional Model," *AIAA Journal*, Vol. 41, No. 7, July 2003, pp. 1389–1391.

[28] Adrian, R. J., and Moin, P., "Stochastic Estimation of Organized Turbulent Structure: Homogeneous Shear Flow," *Journal of Fluid Mechanics*, Vol. 190, May 1988, pp. 531–559. doi:10.1017/S0022112088001442

[29] Noack, B., Tadmor, G., and Morzynski, M., "Actuation Models and Dissipative Control in Empirical Galerkin Models of Fluid Flows," *Proceedings of the 2004 American Control Conference*, American Automatic Control Council, Evanston, IL, June 2004, pp. 5722–5727.

[30] Cattafesta, L. N., Williams, D. R., Rowley, C. W., and Alvi, F. S., "Review of Active Control of Flow-Induced Cavity Resonance," AIAA Paper 2003-3567, June 2003.

[31] Rowley, C., and Williams, D., "Dynamics and Control of High-Reynolds-Number Flow over Open Cavities," *Annual Review of Fluid Mechanics*, Vol. 38, Jan. 2006, pp. 251–276. doi:10.1146/annurev.fluid.38.050304.092057

[32] Yan, P., Debiasi, M., Yuan, X., Little, J., Özbay, H., and Samimy, M., "Closed-Loop Linear Control of Cavity Flow," *AIAA Journal*, Vol. 44, No. 5, May 2006, pp. 929–938. doi:10.2514/1.14873

[33] Kim, K., Debiasi, M., Schultz, R., Serrani, A., and Samimy, M., "Dynamic Compensation of a Synthetic Jetlike Actuator for Closed-Loop Cavity Flow Control," *AIAA Journal*, Vol. 46, No. 1, Jan. 2008, pp. 232–240. doi:10.2514/1.30095

[34] Caraballo, E., Little, J., Debiasi, M., and Samimy, M., "Development and Implementation of an Experimental Based Reduced-Order Model for Feedback Control of Subsonic Cavity Flows," *Journal of Fluids Engineering*, Vol. 129, No. 7, July 2007, pp. 813–824. doi:10.1115/1.2742724

[35] Efe, M. O., and Ozbay, H., "Low Dimensional Modelling and Dirichlet Boundary Controller Design for Burgers Equation," *International Journal of Control*, Vol. 77, No. 10, July 2004, pp. 895–906. doi:10.1080/00207170412331270532

[36] Efe, M. O., Özbay, H., and Samimy, M., "Infinite Dimensional and Reduced Order Observers for Burgers Equation," *International Journal of Control*, Vol. 78, No. 11, Nov. 2005, pp. 864–874. doi:10.1080/00207170500158813

[37] Lehmann, O., Luchtenburg, M., Noack, B., King, R., Morzynski, M., and Tadmor, G., "Wake Stabilization Using POD Galerkin Models with Interpolated Modes," *Proceedings of the 44th IEEE Conference on Decision and Control and 2005 European Control Conference*, IEEE Publishing, Piscataway, NJ, Dec. 2005, pp. 500–505.

[38] Camphouse, R., "Basis Construction for the Design of Boundary Feedback Controls from Reduced Order Models," Air Force Research Lab., Wright–Patterson AFB, OH, TR ADA464776, 2006.

[39] Debiasi, M., and Samimy, M., "Logic-Based Active Control of Subsonic Cavity-Flow Resonance," *AIAA Journal*, Vol. 42, Sept. 2004, pp. 1901–1909. doi:10.2514/1.4799

[40] Little, J., Debiasi, M., Caraballo, E., and Samimy, M., "Effects of Open-loop and Closed-loop Control on Subsonic Cavity Flows," *Physics of Fluids*, Vol. 19, No. 6, June 2007, p. 065104. doi:10.1063/1.2740302

[41] Rowley, C. W., Colonius, T., and Murray, R. M., "Model Reduction for Compressible Flows Using POD and Galerkin Projection," *Physica D*, Vol. 189, Nos. 1–2, Jan. 2004, pp. 115–129. doi:10.1016/j.physd.2003.03.001

[42] Sirovich, L., "Turbulence and the Dynamics of Coherent Structures," *Quarterly of Applied Mathematics*, Vol. 45, No. 3, Oct. 1987, pp. 561–590.

[43] Guezennec, Y. G., "Stochastic Estimation of Coherent Structures in Turbulent Boundary Layers," *Physics of Fluids A, Fluid Dynamics*, Vol. 1, No. 6, 1989, pp. 1054–1060. doi:10.1063/1.857396

[44] Murray, N. E., and Ukeiley, L. S., "Estimation of the Flowfield from Surface Pressure Measurements in an Open Cavity," *AIAA Journal*, Vol. 41, No. 5, 2003, pp. 969–972.

[45] Yuan, X., Caraballo, E., Debiasi, M., Little, J., Serrani, A., Özbay, H., and Samimy, M., "Experimental Results and Bifurcation Analysis on Scaled Feedback Control for Subsonic Cavity Flows," *Proceedings of the 14th Mediterranean Control Conference*, IEEE Publishing, Piscataway, NJ, June 2006, pp. 1–6.

M. Ahmadian
Associate Editor